JOURNAL OF GEOPHYSICAL RESEARCH, VOL. 112, C05032, doi:10.1029/2006JC003698, 2007

On long baroclinic Rossby waves in the tropical North Atlantic observed from profiling floats

P. C. Chu,[1] L. M. Ivanov,[1,3] O. V. Melnichenko,[1,2] and N. C. Wells[4]

Received 11 May 2006; revised 4 December 2006; accepted 26 December 2006; published 16 May 2007.

[1] Argo float data (subsurface tracks and temperature profiles collected from March 2004 through May 2005) are used to detect signatures of long Rossby waves in the velocity of the currents at 1000-m depth and temperature, between the ocean surface and 950 m, in the zonal band of 4°N–24°N in the tropical North Atlantic. Different types of long Rossby waves (with the characteristic scales between 1000 and 2500 km) are identified in the western [west of the Mid-Atlantic Ridge (MAR)] and eastern [east of the MAR] subbasins. Along-shore wind fluctuations and an equatorially forced coastal Kelvin wave were found to be responsible for the excitation of annual- and semiannual-propagating Rossby waves in the eastern subbasin. These waves are transmitted along a waveguide formed by the African shelf and the MAR. The speed of their propagation varies in magnitude and direction because of bottom topography and irregularity of the coastline. Unstable standing Rossby waves with annual and semiannual periods are shown in both the subbasins. All unstable waves, decaying, radiate shorter free Rossby waves propagating both westward and northwestward, with speeds of up to 10 cm/s. The standing Rossby waves are probably excited by the wind-driven Ekman pumping alone or in combination with linear and nonlinear resonance mechanisms. The additional analysis of subsurface float tracks from May 2005 through May 2006 supports the obtained results.

Citation: Chu, P. C., L. M. Ivanov, O. V. Melnichenko, and N. C. Wells (2007), On long baroclinic Rossby waves in the tropical North Atlantic observed from profiling floats, *J. Geophys. Res.*, *112*, C05032, doi:10.1029/2006JC003698.

1. Introduction

[2] The tropical region of the North Atlantic (between 4° and 24°N) is known to be an important transition zone between dynamically very different equatorial and subtropical domains. This region can be regarded as the gateway of the North Atlantic for the shallow and deep waters that enter or leave this basin as a part of the thermohaline Meridional Overturning Circulation (MOC). Therefore the physical mechanisms for the water mass, heat, and salt transports through and within this region play an important role in climate [*Chang et al.*, 2005].

[3] Considerable spatial and temporal variability is superimposed on the mean currents in the tropical Atlantic, where the seasonal cycle is the largest signal. This variability is clearly observed in the upper layer of the ocean [*Stramma and Schott*, 1999].

[4] Although the seasonal flow variability is less obvious for the intermediate and deep layers, due to the lack of long observation series and sparse observation coverage, a number of researchers have reported on seasonal reversals of zonal flows at intermediate depths observed close to the equator [*Schott et al.*, 1998; *Gouriou et al.*, 1999; *Molinari et al.*, 1999; *Richardson and Frantantoni*, 1999; *Schmid et al.*, 2003, 2005]. They assumed that planetary waves cause the variability. For example, *Molinari et al.* [1999] detected two current reversals that propagated westward with a speed of about 15 cm/s at intermediate depths between the equator and 3°N. Waves with the same phase speed and seasonal periodicity are found in an eddy-resolving ocean model [*Böning and Schott*, 1993]. *Yang* [1999] proposed that a linkage between the high-latitude and tropical ocean is set by Kelvin and Rossby wave propagation.

[5] These and other results (not discussed here) indicate that the planetary (Kelvin and Rossby) waves may be potential candidates, which are responsible for linkages between the tropical and high-latitude Atlantic. To better understand their nature, we need to (1) detect these waves from observations which are typically sparse and from results obtained using numerical models of different complexity and (2) estimate wave characteristics (wakes, phase speeds, and scales etc.).

[6] The present study focuses on the long Rossby waves, using the Argo float tracks and temperature profiles to reconstruct a spatial structure of the mid-depth circulation and understand its variability. There are three sources of knowledge about these waves and their variability associated with the large-scale atmospheric variability in the tropical Atlantic.

[7] First, strong planetary wave variability is evident from Ocean Topography Experiment (TOPEX)/POSEIDON

[1]Department of Oceanography, Naval Postgraduate School, Monterey, California, USA.
[2]Marine Hydrophysical Institute, Sevastopol, Ukraine, USA.
[3]University of Southern California, Los Angeles, California, USA.
[4]Southampton Oceanography Center, Southampton, United Kingdom.

0148-0227/07/2006JC003698$09.00

altimetry-derived sea-surface anomaly [*Chelton and Schlax*, 1996; *Osychny and Cornillon*, 2004], Advanced Very High Resolution Radiometer (AVHRR) sea-surface temperature (SST) [*Cipollini et al.*,1997; *Hill et al.*, 2000], and ocean color [*Cipollini et al.*, 2001; *Killworth et al.*, 2004]. These observations are extremely important for better understanding and for the estimation of the kinematic features of Rossby beams (or wave packets) propagating across the Atlantic. However, the satellite data do not give too much information about vertical structure of baroclinic waves.

[8] Second, considerable progress has also been achieved in recent numerical model simulations [e.g., *Herrmann and Krauss*, 1989; *Brandt and Eden*, 2005]. Using an Ocean General Circulation Model for the North Atlantic with annual forcing, *Böning and Schott* [1993] and *Böning and Kröger* [2005] found that the deep current fluctuations of O (5 cm/s), which appear to be consistent with long equatorial Rossby waves dynamics, are induced by the seasonal cycle of the wind stress forcing. Using an idealized regional model for the tropical Atlantic Ocean, *Jochum and Malanotte-Rizzoli* [2003] found that the transport of the Antarctic Intermediate Water along the equator is dominated by the Rossby wave activity related to the annual cycle of wind stress. Using idealized and realistic high-resolution primitive equation models of the equatorial Atlantic Ocean, *Thierry et al.* [2004] found that annual velocity fluctuations are dominated by the lowest odd-meridional mode Rossby beam, which, after being generated by the reflection of the directly wind-driven shallow Kelvin beam at the eastern boundary, propagates westward and downward.

[9] Third, deep hydrographic and velocity measurements from conductivity temperature depth (CTD), moorings, and drifting buoys provide some evidence of Rossby wave variability in the tropical Atlantic. Although many investigators [*Freeland et al.*, 1975; *Richardson and Frantantoni*, 1999; *Molinari et al.*, 1999; *Schmid et al.*, 2003] have shown the capability of subsurface floats to detect the Rossby wave wakes, sparseness of observations and mathematical procedures used to analyze the data did not allow them to reconstruct spatiotemporal structures of Rossby and Kelvin waves.

[10] The objectives of the proposed study are (1) to demonstrate the capability of the Argo float data in detecting the spatiotemporal structure of long baroclinic Rossby waves in a tropical region between 4° and 24°N in the North Atlantic; (2) to estimate the kinematic characteristics of Rossby waves; and (3) to find possible mechanisms of their generation.

[11] The paper is organized as follows. After describing the data (Argo float observations and National Center for Environmental Prediction/National Center for Atmospheric Research (NCEP/NCAR) wind reanalysis product) in section 2, a mathematical procedure applied to the Argo data to obtain long Rossby wave variability is discussed in section 3, where estimations of accuracy of the reconstructed mid-depth currents and temperature from the data can also be found. Results of the reconstruction for currents and temperature are presented in sections 4 and 5. The annual and semiannual Rossby waves are analyzed in sections 6 and 7. Section 8 includes results of additional analysis of subsurface float tracks from May 2005 through May 2006. A summary of the obtained results and conclusions is provided in section 9.

2. Data

2.1. Argo Float Data

[12] Between March 2004 and May 2005, over 60,000 float days (cumulative) of data were collected in the North Atlantic mostly at three parking depths: 1000, 1500, and 2000 m [http://www.Argo.ucsd.edu and http://Argo.jcommops.org]. Our analysis involves all available Argo temperature profiles and subsurface displacements of floats parked only at 1000 and 1500 m. Floats parked at 2000 m and shallower than 1000 m as well as those for which there was no information on parking depth were excluded from the analysis. Typical float tracks are shown in Figure 1a.

[13] The following sources of uncertainty in Argo float data lead to computational errors in the velocity estimate:

[14] (1) The data were extracted from floats parked at two different levels, 1000 and 1500 m, and grouped together at 1000 m, neglecting vertical shear. This error is absent for the reconstruction of currents in the tropical region between 4° and 24°N, where Argo floats were, in general, parked at the 1000-m level.

[15] (2) The vertical shear causes an increase or decrease of the real distance between the points of ascending from and descending to the parking depth.

[16] (3) The sequence of float trajectory segments (tracks) only approximates the real Lagrangian paths. We may fix float positions after their ascent to the ocean surface and before their descent to the parking depth only.

[17] (4) Preliminary computations (not shown here) demonstrated that high-resolution elements of mid-depth circulation in the North Atlantic, such as the northern recirculation gyre in the western North Atlantic, Deep Western Boundary Current (DWBC) [*Reid*, 1994], the systems of eastward and westward zonal flows in the equatorial Atlantic [*Stramma and Schott*, 1999] are also detectable using the Argo float data. However, such a resolution is not available for the whole North Atlantic, and high-energetic mesoscale eddies as well as narrow boundary currents should be classified as "noise" and removed from the analysis or parameterized.

[18] (5) There are large spatial gaps [from 200 to 600 km] in Argo float observation coverage.

[19] The quality of temperature observations is higher than the velocity ones with fewer spatial gaps. Here temperature profiles from all floats including the ones parked shallower than 1000 m and deeper than 1500 m and the floats parked at unknown depths were used to reconstruct three-dimensional temperature field from the ocean surface to 950 m. Figure 1b demonstrates typical observation coverage for a 2-month observation period (October–November 2004). Measurement errors caused by temperature sensors seem to be not too large to affect considerably the vertical structure of temperature profiles. An interested reader can find the detailed discussion on navigation errors and measurement errors caused by temperature sensors in http://Argo.jcommops.org.

2.2. Quality Control of Data

[20] Three quality control steps are performed to identify and remove temperature profiles corrupted by large measurement errors.

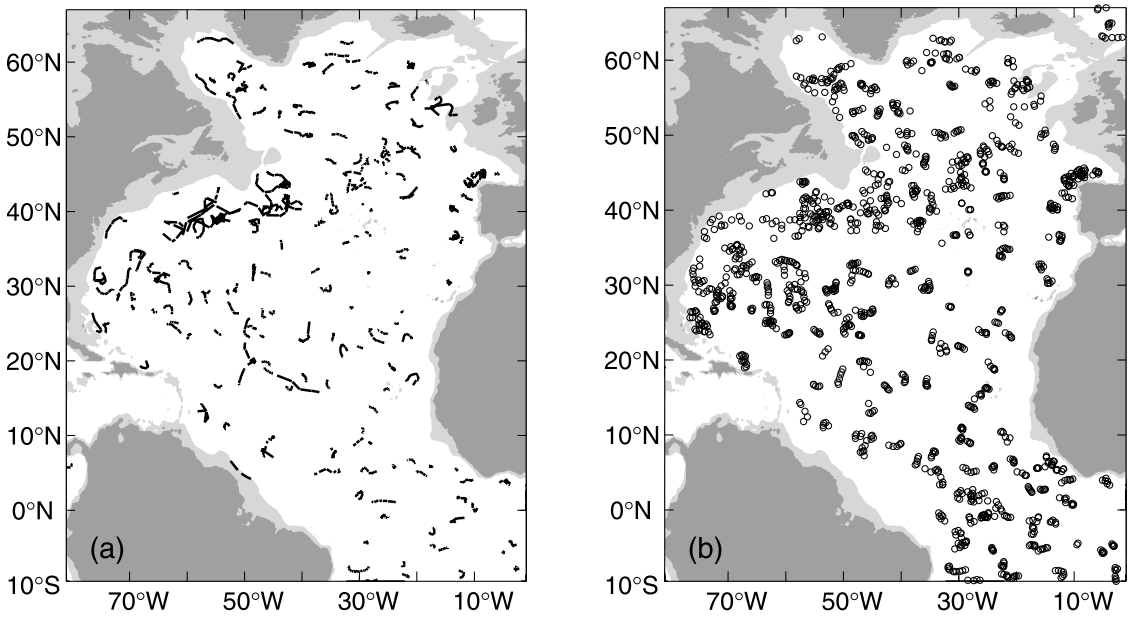

Figure 1. ARGO observation coverage of the North Atlantic in October–November 2004: (a) subsurface tracks of floats parked at 1000 and 1500 m and (b) all float positions where temperature profiles were measured.

[21] (1) Explicitly absurd profiles were removed after a visual inspection.

[22] (2) A portion of temperature profiles, which were outside of the prescribed accuracy of the climatic data [*Levitus et al.*, 1998], were also excluded from further analysis.

[23] (3) Temperature snapshots computed by the Optimal Spectral Decomposition (OSD) method [*Ivanov et al.*, 2001; *Chu et al.*, 2003, 2004] should not show explicit outbreaks in temperature structure. Any temperature profile contributing to such outbreaks was subject to removal.

[24] A parking depth for each Argo float was extracted from a "meta" file as the variable "PARKING_PRESSURE" (http://www.Argo.ucsd.edu and http://Argo.jcommops.org). To control the parking depth, the variable "PRES" (a pressure measured along the float trajectory) from a file containing float trajectory data was used. Most floats launched in the area of interest have measured this variable.

[25] Positioning errors due to velocity shear in the upper ocean layer were corrected as described in Appendix A.

2.3. NCEP/NCAR Wind

[26] To understand correlations between wind and observed variability in currents and temperature, the NCEP/NCAR wind reanalysis product provided by the National Oceanic and Atmospheric Administration (NOAA)-Cooperative Institute for Research in Environmental Sciences (CIRES) Earth System Research Laboratory (ESRL)/Physical Sciences Division (PSD) Climate Diagnostics Branch, Boulder, Colorado is used [http://www.cdc.noaa.gov/]. The wind stress and wind stress curl were directly computed with a spatial resolution of 2.5°. Preliminary computations (not shown here) indicate that such spatial resolution is satisfactory to understand effects of atmosphere-ocean interactions on the basin-scale variability in the tropical North Atlantic.

3. Reconstruction Procedure

3.1. Basic Equations

[27] Following the studies of *Eremeev et al.* [1992] and *Chu et al.* [2003] a quasi-geostrophic velocity $\hat{\mathbf{U}}(\mathbf{x}_\perp, t)$ in the zonal band 4°–24°N (the domain Ω_1 shown in Figure 2) at the vertical level $z = 1000$ m is represented in the form of a parameter-weighted sum of the harmonic $Z_s(\mathbf{x}_\perp)$ and basis $\Psi_k(\mathbf{x}_\perp)$ functions as

$$\hat{\mathbf{U}}(\mathbf{x}_\perp, t) = \sum_{s=1}^{S} a_s(t)[\mathbf{k} \times \nabla Z_s(\mathbf{x}_\perp)] + \sum_{k=1}^{K} b_k(t)[\mathbf{k} \times \nabla \Psi_k(\mathbf{x}_\perp)], \tag{1}$$

[28] Hereafter, $\hat{\mathbf{U}} = (\hat{U}_1, \hat{U}_2)$; the subscript '$i$' indicates zonal ($i = 1$) and meridional ($i = 2$) components; $\{\mathbf{x}_\perp = (\varphi, \lambda), z\}$ is a right-hand coordinate system with φ as the latitude, λ as the longitude, and z as positive upward; $\mathbf{k}$ is the positive normal to the surface $z = -1000$ m, and $\nabla = (\nabla_\varphi, \nabla_\lambda)$ is the horizontal gradient operator.

[29] A set of harmonic functions Z_s is introduced to account for multiconnection features of Ω (i.e., existence of islands) and/or disconnected rigid boundaries (if applicable).

[30] Temperature fields are reconstructed in the whole North Atlantic to the north of 4°N (the domain Ω_2 shown in Figure 2). Temperature at any point of this area at any vertical level z is decomposed [*Ivanov et al.*, 2001; *Chu et al.*, 2004] as

$$\hat{T}(\mathbf{x}_\perp, z, t) = T_{\mathrm{cl}}(\mathbf{x}_\perp, z) + \sum_{m=1}^{M} c_m(t, z)\Xi_m(\mathbf{x}_\perp, z), \tag{2}$$

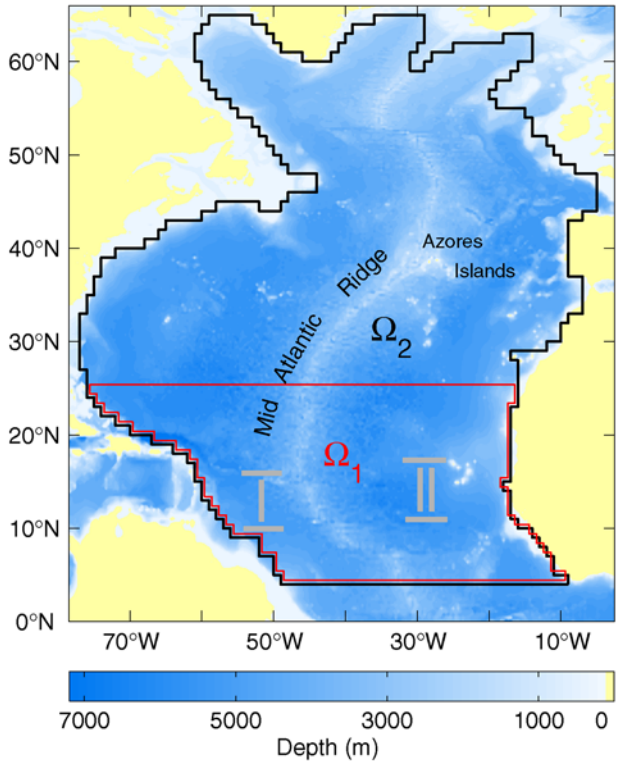

Figure 2. Domains where the mid-depth currents and temperature fields are reconstructed. The boundaries of Ω_1 and Ω_2 are red and black lines, respectively. The Mid-Atlantic Ridge divides the tropical region into the western and eastern subbasins labeled as I and II, respectively.

where $\Xi_m(\mathbf{x}_\perp, z)$ are appropriate basis functions, and $T_{cl}(\mathbf{x}_\perp, z)$ is the climatic temperature [*Levitus et al.*, 1998].

[31] The basis functions $\Psi_k(\mathbf{x}_\perp)$ and $\Xi_m(\mathbf{x}_\perp, z)$ and harmonic functions $Z_s(\mathbf{x}_\perp)$ are assumed to be a priori determined such that the velocity and temperature satisfy appropriate boundary conditions. All details of such calculations are given in Appendix B. The weight coefficients $a_1, \ldots, a_S$; $b_1, \ldots, b_K$; and $c_1, \ldots, c_M$ in equations (1) and (2) are calculated from the Argo data using a variation technique. Subsurface velocities $\mathbf{U}_p$ computed along Argo float tracks and centered at their midpoints $\mathbf{x}_\perp^p$ and temperature measurements at 10 different levels ranging from 50 to 950 dB with a 100-dB resolution are used to estimate these coefficients. When the spectral coefficients have been calculated, equations (1) and (2) are used again to project the velocity and temperature on a regular ($1^\circ \times 1^\circ$) grid. That finishes the reconstruction process.

3.2. Optimal Solution

[32] The key problem of the reconstruction process is how to select the optimal solution which (1) is closest to a "true" solution corresponding to an unknown ocean state, (2) should be robust on the given observation sampling, and (3) tends to the "true" solution as the variance of observation noise $\sigma^2 \to 0$. Following the studies of *Ivanov et al.* [2001] and *Chu et al.* [2003, 2004], the optimal solution with such features can be found using the OSD method. If the optimal solution with such features does not exist or seems to be absurd, a new optimal solution must be specified using additional a priori knowledge on the true ocean state.

[33] The optimal solution minimizes the sum of squared residuals between the reconstruction ($\hat{\mathbf{U}}$, $\hat{T}$) and observations ($\mathbf{U}_p$, $T_p | p = 1, \ldots, P$) at P float locations:

$$J^{-1}(K,P)\left[\left\|\hat{U}-U_p\right\|^2+\left\|\hat{V}-V_p\right\|^2\right] \to \min, \tag{3}$$

$$J^{-1}(M,P)\left\|\hat{T}-T_p\right\|^2 \to \min, \tag{4}$$

which are the subject to the constraints

$$J(h,P) = 1 - P^{-1/2}[h(\ln P/h + 1) - \ln(1-\chi)]^{-1/2}. \tag{5}$$

Here $\chi = 0.95$, h is a truncation number (K or M), the norm notation $\|\cdot\|$ corresponds to the usual L_2 norm.

[34] The optimal solution is specified by choice of truncation numbers K_{opt} and M_{opt} through the constraint J [*Vapnik*, 2006]. All solutions obtained with the number of basis functions larger than the optimal ones are supposed to be unphysical (too large contribution of measurement noise and high-frequency currents). On the other hand, model (1) and (2) is assumed to be not satisfactory to fit observations if $K < K_{opt}$ and $M < M_{opt}$.

[35] Nonlinear least-squares minimization problem (3)–(5) is solved through the Levenberg-Marquardt iterative method [*Engl et al.*, 1996] to determine the optimal values of $a_1, \ldots, a_S$; $b_1, \ldots, b_K$; $c_1, \ldots, c_M$, K_{opt}, and M_{opt}. Then, the mid-depth currents (temperature) are recalculated at any point in Ω_1 (Ω_2) including observation-free areas.

[36] We illustrate how a long-lived (coherent) circulation structure may be extracted from the noisy Argo data by the OSD. The data collected during October–December 2004 are taken as an example.

[37] Current velocities computed along the original (non-smoothed) Argo tracks in November–December 2004 are shown in Figure 3a as red arrows. A strong contribution from intensive eddies, such as that shown in inset B, narrow jets, and measurement errors is clearly identified here. Visually, the velocity pattern corresponding to the original data looks quite chaotic, and there are 500- to 600-km spatial gaps in observation coverage.

[38] To understand the reconstruction skill for such data, we applied three criteria: (1) the formal mean square error (the reconstruction error) computed by the "laminar ensemble" technique [*Turchin et al.*, 1971], (2) statistics of angle (α) between the reconstructed and observed velocity at float locations, and (3) stability degree of the reconstructed snapshot on observation sampling [*Perry and Chong*, 1987].

[39] OSD applied directly to the original data ($K_{opt} = 18$) clearly reproduces a two-gyre flow structure (Figure 3a), which was masked by strong noise in the original data. The maximum reconstruction errors of 16% and 35% are observed in the eastern part of the North Atlantic and over the Mid-Atlantic Ridge (MAR) near 16°N, respectively. The angle α is less than 45° for 48% of comparisons (inset A). The OSD automatically filtrates a contribution from obser-

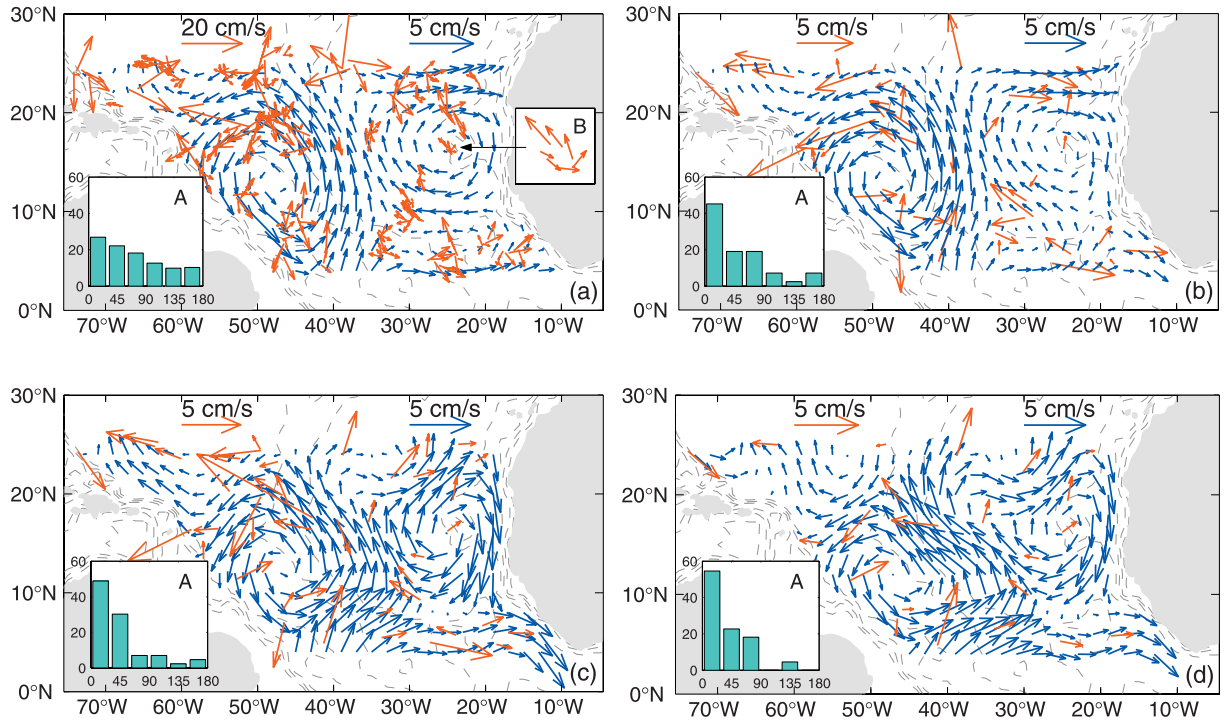

Figure 3. Sensitivity of the reconstructed circulation patterns to filtration of the original data: OSD is applied to (a) the original data (November–December 2004); (b) the original data (November–December 2004) filtered with a 2-month window; (c) the original data (October–December 2004) filtered with a 3-month window; and (d) the original data (October–December 2004) filtered by 4° × 4° bin averaging; blue and red arrows correspond to the reconstructed circulation and original/filtered data. For α histograms (insets A) the x axes is the angle α and the y axes is the number of comparisons (%), as described in section 3.2.

vations, for which α is larger than 90°. However, there is no guarantee that aliasing of errors due to signals at subsampled frequency/wavelength scales did not distort the reconstructed circulation pattern.

[40] A common procedure to avoid aliasing errors is to use low-pass filters before the sampling process. Two simple filters were applied to the original float data: averaging over 4° × 4° spatial bins and a low-frequency temporal filter with the Parzen window h_f [*Yaglom*, 1986; *Collins et al.*, 2004].

[41] Results for OSD reconstruction from the Argo data preliminary filtered by the Parzen window are shown in Figures 3b (h_f = 2 months) and 3c (h_f = 3 months). In both cases, α histograms are sharp, with α less than 45° for 78%–80% of comparisons. Flow skeletons are also robust relative to the window width. Gyre centers are highly stable, and their mean shift due to sampling error is limited by 100 km. Therefore we conclude that the reconstructed pattern is statistically significant. However, the mean reconstruction error is slightly larger for stronger filtration with h_f = 3 months.

[42] The bin average produced a new sampling representing a set of smoothed velocities related to centers of float clusters embedded into appropriate bins (Figure 3d). Applying OSD to these smoothed velocities, we obtained a large-scale circulation structure (Figure 3d), which is similar to that shown in Figure 3c. The reconstruction skill for the pattern in Figure 3d seems to be the same as in Figure 3c. The formal reconstruction error increases in the eastern part of the North Atlantic up to 40%, but a number of outliers for α became considerably smaller. The angle α is less than 45° for 63% of comparisons (inset A, Figure 3b). No shift of the gyre centers is observed in comparison with Figures 3a–3c.

[43] These computations clearly show that a part of signal at subsampled wavelength scales is pure white noise. Analyzing residuals between the original velocities and their averaged counterparts, we identified these signals as quasi-isotropic non-Gaussian white noise with zero mean, standard deviation of 5.312 cm/s, skewness of 0.034, and kurtosis of 6.34.

[44] We suppose that the reconstructed two-gyre flow structure shown in Figure 3a or 3b can be taken as the optimal solution by a number of reasons. It is less smoothed, robust to the observation sampling, and weakly distorted by signals at subsampled frequency/wavelength scales.

[45] To reduce noise impact on the Argo float data, subsurface velocities were jointed within 2-month periods, and 14 overlapping intervals between March 2004 and May 2005 were created as March–April 2004; April–May 2004; May–June 2004; ...; and April–May 2005. The reconstruction procedure was separately applied to each sampling period that resulted into 14 snapshots assigned to represent the midpoints of these intervals. These snapshots were dynamically consistent, and the lifetime for the reconstructed coherent flow structures exceeded 6 months. The

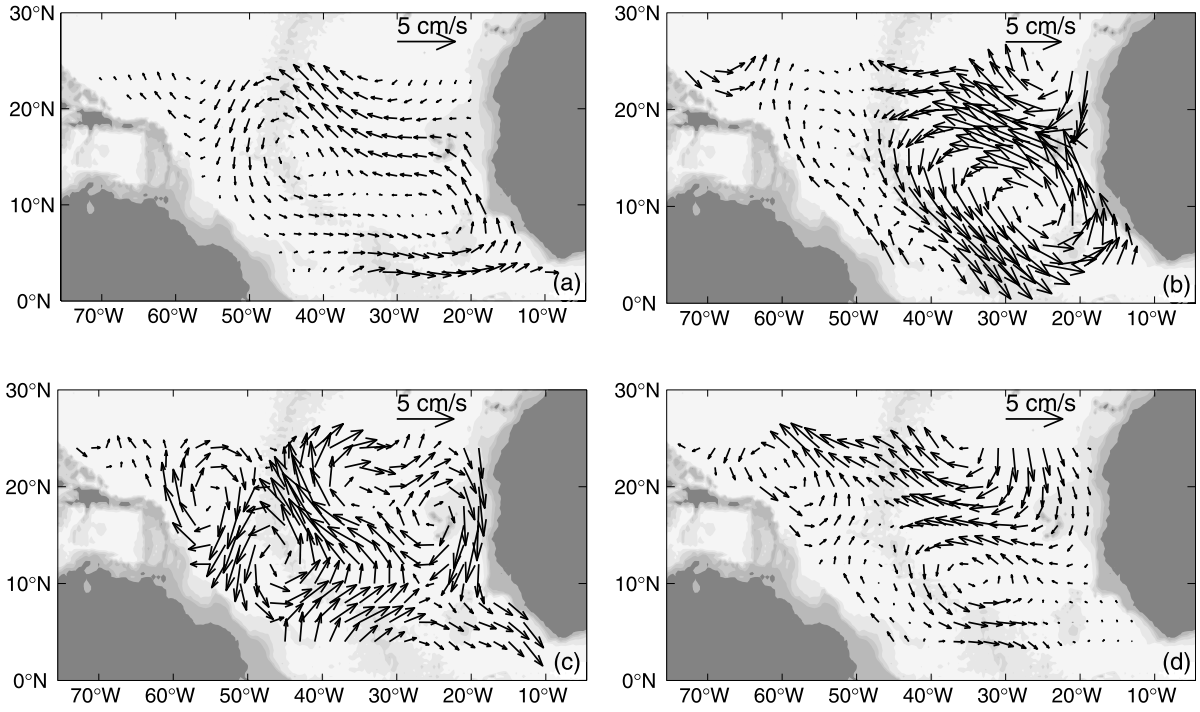

Figure 4. Reconstructed mid-depth currents (a) averaged over April 2004–April 2005 and from the data collected (b) within June–July 2004; (c) within October–November 2004; and (d) within March–April 2005.

optimal truncation number K_{opt} was 18 through all 14 snapshots.

[46] The approach discussed above was also used to reconstruct a set of two-dimensional temperature fields at 10 different levels ranging from 50 to 950 dB with a 100-dB resolution. Temperature data are much better because spatial gaps in float coverage are smaller, and the level of noise corrupting the data is lower than for velocity observations. Therefore monthly temperature snapshots were reconstructed in the domain to the north of 4°N. Our study uses only temperature fields in the zonal band from 4° to 24°N. The estimated optimal truncation number M_{opt} in decomposition (2) equals to 38. We specified temperature distortions as quasi-Gaussian white noise with zero mean and standard deviation of 0.1°C.

4. Mid-depth Circulation

[47] The annual mean circulation pattern, shown in Figure 4a, is characterized by an elongated cyclonic gyre with velocities in the core of less than 2 cm/s, which does not correspond to the schematic flow diagram for the mid-depth layer (500–1160 m) proposed by *Stramma and Schott* [1999] (see, also, the work of *Schmid et al.* [2003]). However, a spatial pattern corresponding to a cyclonic flow approximately around the center of the Guinea dome is clearly seen in Figure 4a. That agrees, for example, with *Eimoussaoui et al.* [2005] who observed the quasi-permanent cyclonic flow of the Guinea dome at the same depth and deeper.

[48] A sequence of average bimonthly snapshots for velocity, shown in Figures 4b–4d, indicates a superposition of eddy-wave-like perturbations (mainly cyclonic rotation) propagating northwestward and westward from the eastern tropical North Atlantic. These perturbations affect the mid-depth flow along the African coast and probably the Intermediate Western Boundary Current (IWBC). That should result in reversals for boundary currents on seasonal timescales.

[49] For example, the flow along the African coast directed northwest up to 16°N in spring and summer reverses to the south in fall. Evidence for this result can also be found in the studies of *Eimoussaoui et al.* [2005], *Fratantoni and Richardson* [1999], and others. The resolution of the reconstructed fields is too low to analyze narrow boundary currents, such as IWBC. Therefore fall-winter reverses of IWBC from northwestward to southeastward, which may be observed south of 15°N [*Stramma and Schott*, 1999], are not explicitly extracted from our results.

[50] The perturbations shown in Figures 4b–4d have complex spatiotemporal structure and seem to be formed by currents with various characteristic scales and, probably, differently forced. However, the most energetic perturbation in this wave train travels across the Atlantic with a speed of 10–15 cm/s, which is comparable to the zonally averaged phase speed of long baroclinic Rossby waves calculated from the linear theory [*Pedlosky*, 1987] and estimated from TOPEX/POSEIDON sea-surface anomaly [see *Chelton and Schlax*, 1996; *Polito and Cornillon*, 1997; *Osychny and Cornillon*, 2004].

[51] Our computations (Figures 4b–4d) demonstrate frequent changes in the structure of the perturbations associated with their merger, decay, and dissipation and that the perturbations propagate rather northwestward than westward as free long Rossby waves. To explain these transformations in the wave train and understand the nature

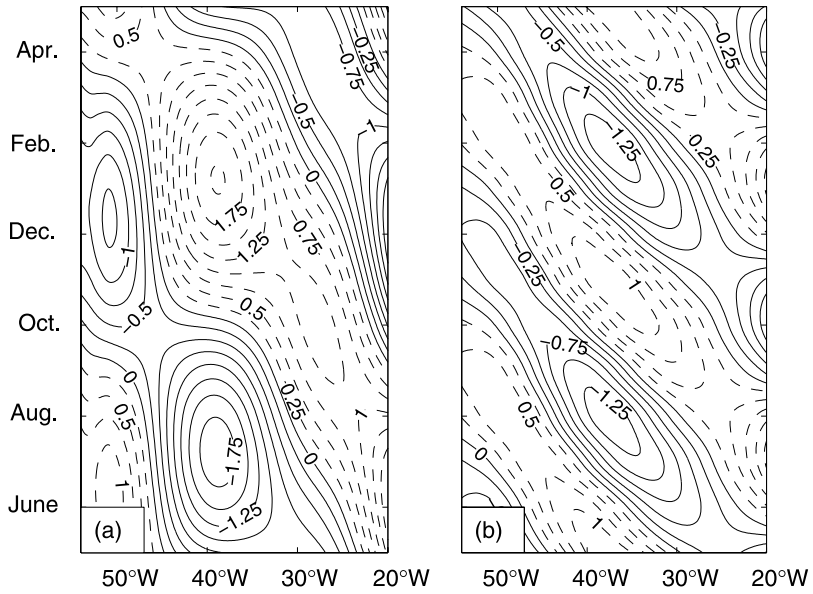

Figure 5. Time-longitude diagrams of meridional velocity (cm/s) along 11°N: (a) annual signal and (b) semiannual signal.

of the wave perturbations, a simple empirical analysis based on a spectral decomposition of the reconstructed signal and time-longitude sections (Hovmöller diagrams) will be applied.

[52] The annual and semiannual cycles are the largest ocean-atmosphere signals in the tropical Atlantic. Between the equator and 20°N they contain up to 60%–80% of the total variance in surface elevation [*Gerdes and Wübber*, 1991; *Schouten et al.*, 2005]. Therefore it seems to be reasonable to detect annual and semiannual variability in the mid-depth circulation and temperature reconstructed within the 14-month observation period.

[53] The stream function $\hat{\psi}$ of the reconstructed circulation is decomposed into the mean background ($\bar{\psi}$) and sum of the annual (ψ_1) and semiannual (ψ_2) oscillations

$$\hat{\psi} \approx \bar{\psi}(\mathbf{x}_\perp) + \psi_1(\mathbf{x}_\perp, t) + \psi_2(\mathbf{x}_\perp, t), \tag{6}$$

$$\begin{aligned}\psi_1(\mathbf{x}_\perp, t) = &\sum_{s=1}^{2} A_{\omega_1,s} \cos\left(\omega_1 t + \theta_{\omega_1,s}\right) Z_s(\mathbf{x}_\perp) \\ &+ \sum_{k=1}^{K_{\text{opt}}} B_{\omega_1,k} \cos\left(\omega_1 t + \vartheta_{\omega_1,k}\right) \Psi_k(\mathbf{x}_\perp),\end{aligned} \tag{7}$$

$$\begin{aligned}\psi_2(\mathbf{x}_\perp, t) = &\sum_{s=1}^{2} A_{\omega_2,s} \cos\left(\omega_2 t + \theta_{\omega_2,s}\right) Z_s(\mathbf{x}_\perp) \\ &+ \sum_{k=1}^{K_{\text{opt}}} B_{\omega_2,k} \cos\left(\omega_2 t + \vartheta_{\omega_2,k}\right) \Psi_k(\mathbf{x}_\perp),\end{aligned} \tag{8}$$

where T_0 = 12 months; $\omega_1 = 2\pi/T_0$; $\omega_2 = 4\pi/T_0$; $A_{\omega,s}$, $B_{\omega,k}$; and $\theta_{\omega,s}$, $\vartheta_{\omega,k}$ are the amplitudes and initial phases, respectively; $\bar{\psi}$ is the mean stream function over a 1-year period.

[54] Because of the short observation sampling (14 months), the oscillation period T_0 is assumed to be known exactly, and only the time t_0, which indicates the start of the seasonal cycle within the observation period, is determined from the following minimization problems:

$$J_s = \int_{t_o}^{t_o+T_o} \left[a_s(t) - \sum_{\omega=\omega_1,\omega_2} A_{\omega,s} \cos\left(\omega t + \theta_{\omega,s}\right) \right]^2 \mathrm{d}t \to \min, \tag{9}$$

$$I_k = \int_{t_o}^{t_o+T_o} \left[b_k(t) - \sum_{\omega=\omega_1,\omega_2} B_{\omega,s} \cos\left(\omega t + \vartheta_{\omega,s}\right) \right]^2 \mathrm{d}t \to \min. \tag{10}$$

This time corresponds to the midpoint of April 2004. In this case, decomposition (6) approximates the reconstructed circulation for any month within April 2004–April 2005 with accuracy not worse than 80%.

[55] Some useful information may be obtained from the analysis of the time-longitude cross-sections for the meridional velocity of annual and semiannual oscillations. For example, Figures 5a and 5b show westward-propagating signals with a phase speed of 8–9 cm/s and wavelength of 2600–3100 km for the annual oscillation (Figure 5a) and a phase speed of 15–16 cm/s and wavelength of 1600–2160 km for the semiannual one (Figure 5b). The wavelengths of propagating perturbations are comparable to the basin scale, and one might hypothesize that the spatial structure and evolution of perturbations should be strongly affected by the MAR and the irregularity of the coastline.

5. Temperature

[56] The annual mean temperature field reconstructed at 950 m is demonstrated in Figure 6a. This figure shows

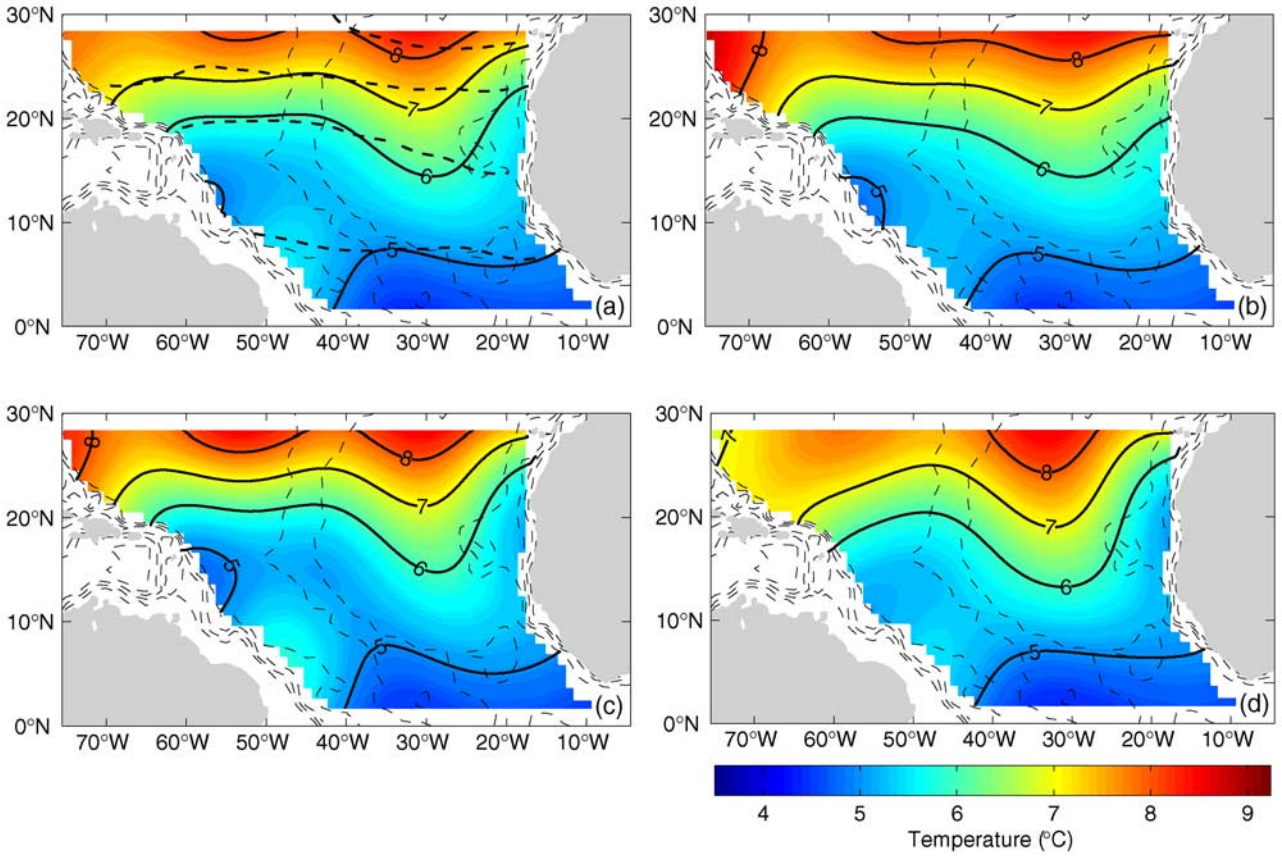

Figure 6. Temperature fields reconstructed at 950 m: (a) averaged over April 2004–April 2005 and Levitus climatology (dashed curves denoting 5°C, 6°C, 7°C, and 8°C isotherms) and monthly (b) for July 2004, (c) November 2004, and (d) April 2005.

(1) enhanced horizontal gradients of the annual mean temperature in the zonal band of 16°–25°N and (2) that cold (defined as Antarctic-originated water in the study of *Jochum and Malanotte-Rizzoli* [2003]) and warm (probably with a contribution of originally Mediterranean water [*Reid*, 1994]) water masses deeply penetrate into the tropical North Atlantic along the coastline of South America and through the center of the eastern subbasin, respectively. The reconstructed annual mean temperature seems to be less smoothed than the climatic temperature in the study of *Levitus et al.* [1998], also shown in Figure 6a.

[57] Monthly temperature snapshots are represented in Figures 6b–6d. A visual inspection of these figures shows that southward heat flux in the eastern subbasin varies at seasonal scales. To understand such variability, temperature at depth z is approximated similarly to equation (6) as

$$\hat{T}(\mathbf{x}_\perp, z, t) \approx \bar{T}(\mathbf{x}_\perp, z) + T_1(\mathbf{x}_\perp, z, t) + T_2(\mathbf{x}_\perp, z, t), \quad (11)$$

$$T_1(\mathbf{x}_\perp, z, t) = \sum_{m=1}^{M_{\text{opt}}} C_{\omega_1, m}(z) \cos\left[\omega_1 t + \chi_{\omega_1, m}(z)\right] \Xi_m(\mathbf{x}_\perp, z), \quad (12)$$

$$T_2(\mathbf{x}_\perp, z, t) = \sum_{m=1}^{M_{\text{opt}}} C_{\omega_2, m}(z) \cos\left[\omega_2 t + \chi_{\omega_{21}, m}(z)\right] \Xi_m(\mathbf{x}_\perp, z), \quad (13)$$

where $C_{\omega_1,m}(z)$, $C_{\omega_2,m}(z)$ and $\chi_{\omega_1,m}(z)$, $\chi_{\omega_2,m}(z)$ are the amplitudes and initial phases, respectively; $\bar{T}$ is the mean temperature over the period from April 2004 through April 2005; T_1 and T_2 are the annual and semiannual oscillations, respectively.

[58] In good agreement with Figure 5, the time-longitude diagrams of annual and semiannual temperature perturbations along 11°N latitude indicate clear westward-propagating wave signals. The annual signal T_1 at 550 m (950 m) shown in Figure 7a (Figure 7c) represents a combination of propagating perturbations dominating between 25° and 55°W (28° and 55°W) and standing perturbations dominating between 20° and 25°W (16° and 28°W). It seems that the traveling annual perturbations are excited at the African coast and then propagate westward at a speed of about 8–9 cm/s. The semiannual signal shown in Figure 7b (Figure 7d) at 550 m (950 m) represents the westward-propagating perturbations across the basin from the African coast to the South America with a phase speed of 16–17 cm/s.

[59] Although westward-propagating perturbations in temperature and velocity are clearly detected in Figures 5 and 7, more accurate estimating of the kinematic characteristics of these perturbations can be done from the analysis of temperature and velocity snapshots reconstructed in con-

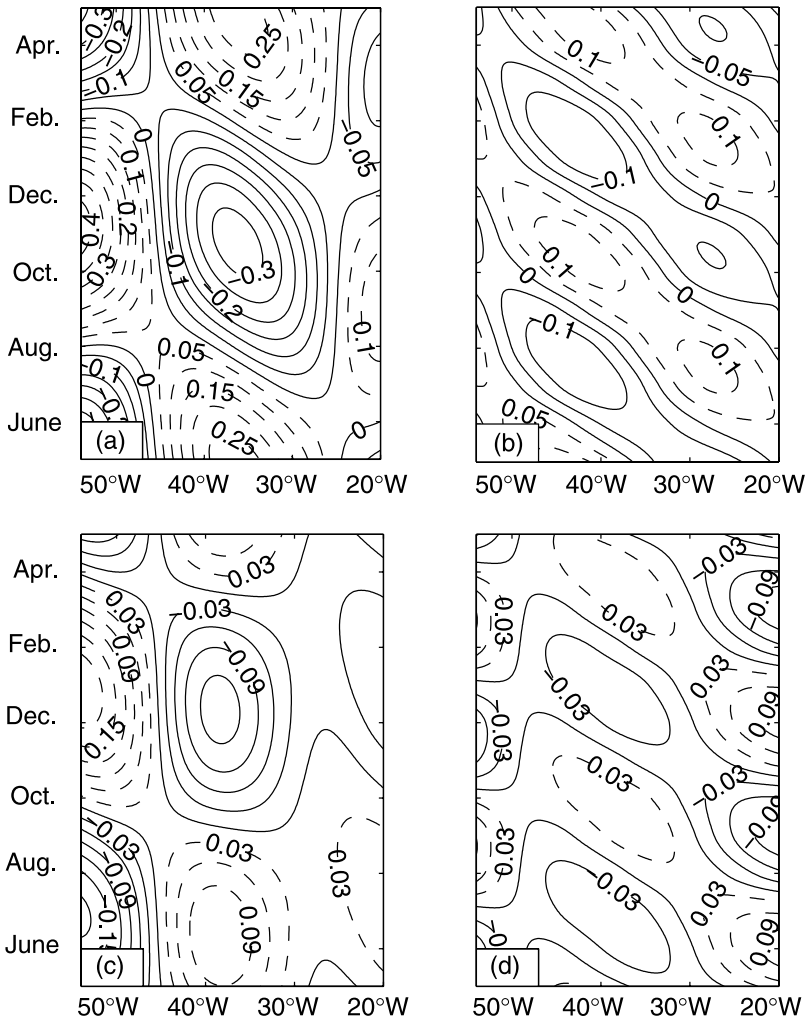

Figure 7. Longitude-time diagrams of the temperature anomaly (°C) along 11°N: annual signal at 550 (a) and 950 m (c); semiannual signal at 550 (b) and 950 m (d).

secutive time moments. Such an analysis is suggested below.

6. Annual Baroclinic Rossby Waves

6.1. Kinematic Characteristics

[60] A sequence of spatial snapshots presented in Figure 8 demonstrates the existence of two annual wave-like perturbations [labeled as A_1 (A_2) and B_1 (B_2)] propagating independently from each other. The perturbation A_1 excited in the eastern subbasin moves mainly northwestward rather than exactly westward as it is predicted by the classical theory of free long linear baroclinic Rossby waves. The magnitude of propagation speed (c_p) varies between 7 and 14 cm/s and is directed along isobaths in May 2004–March 2005.

[61] Approximating the perturbation A_1 by an elliptic-shape wave packet and introducing the main elliptic axes (λ_1, λ_2) (as shown in Figure 8a for the perturbation B_1), we estimate its characteristic length scales along these axes as

$$L_1 \approx 1800 - 2500 \text{ km}, \quad L_2 \approx 1400 - 1500 \text{ km}. \tag{14}$$

[62] Since the kinematic characteristics (the propagation speed, characteristic scales, and period) of the perturbation A_1 are close to appropriate characteristics of the long baroclinic Rossby waves observed in this region from satellite altimetry data [*Osychny and Cornillon*, 2004], we identify the perturbations A_1 as a baroclinic Rossby wave.

[63] The perturbation B_1 observed in the western subbasin is a standing wave during May 2004 to August 2004. The wave characteristic length scales equal to

$$L_1 \approx 2400 - 2600 \text{ km}, \quad L_2 \approx 1100 - 1160 \text{ km}. \tag{15}$$

[64] This wave is unstable and quickly decays (the initial stage of decay is shown in Figure 8b). The wave decay leads to radiation of two shorter waves: a standing wave (labeled by B'_1 in Figure 8b) which quickly dissipates and a new wave (labeled by B''_1 in Figure 8c) moving northwestward with a speed of about 10–11 cm/s.

[65] Although all the perturbations, A_1, B_1, B'_1 and B''_2, may be represented as elliptical-shaped wave packets, their shapes change quite quickly so that

$$\frac{T_0}{L_1}\frac{\partial L_1}{\partial t} > 1, \quad \frac{T_0}{L_2}\frac{\partial L_2}{\partial t} > 1. \tag{16}$$

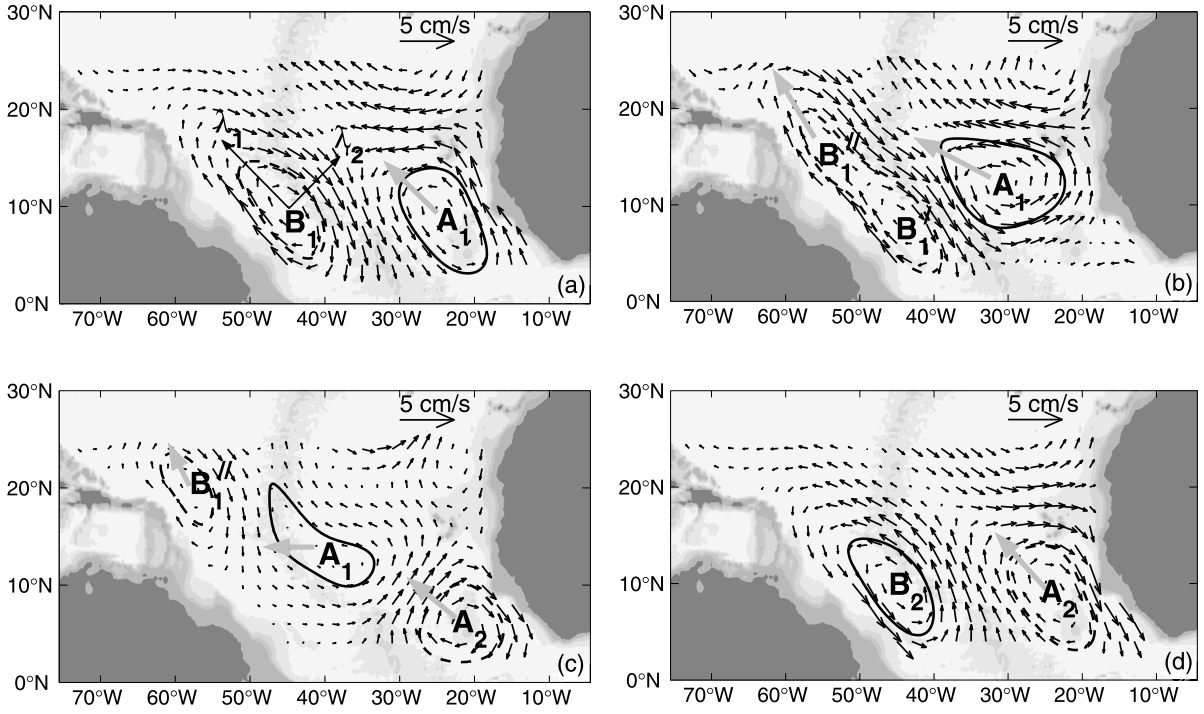

Figure 8. Spatiotemporal structure of the annual currents at 1000-m depth: (a) May–June 2004, (b) July–August 2004, (c) September–October 2004, and (d) November–December 2004. Here the gray arrows show the direction of annual signal propagation.

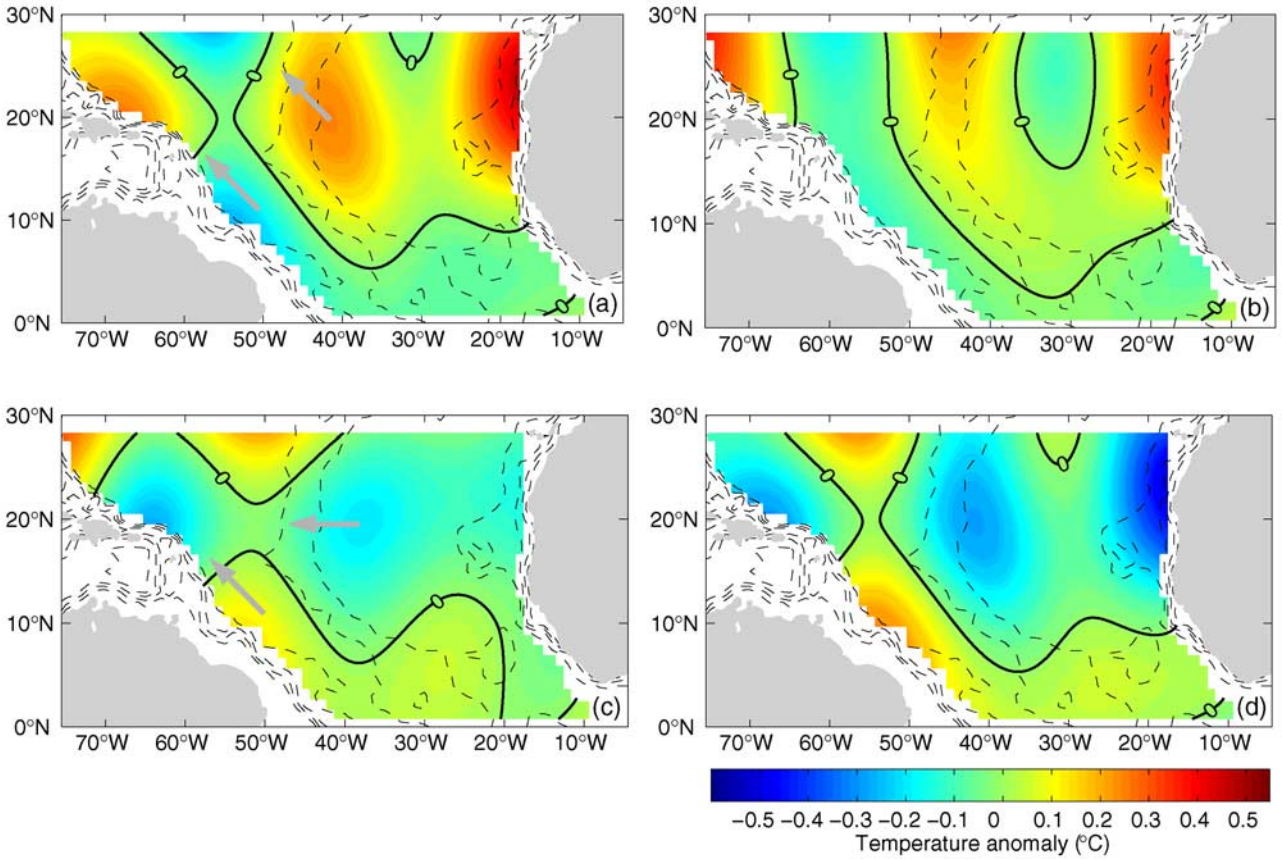

Figure 9. Spatiotemporal structure of annual monthly temperature anomaly at 950-m depth: (a) June 2004, (b) August 2004, (c) October 2004, and (d) December 2004.

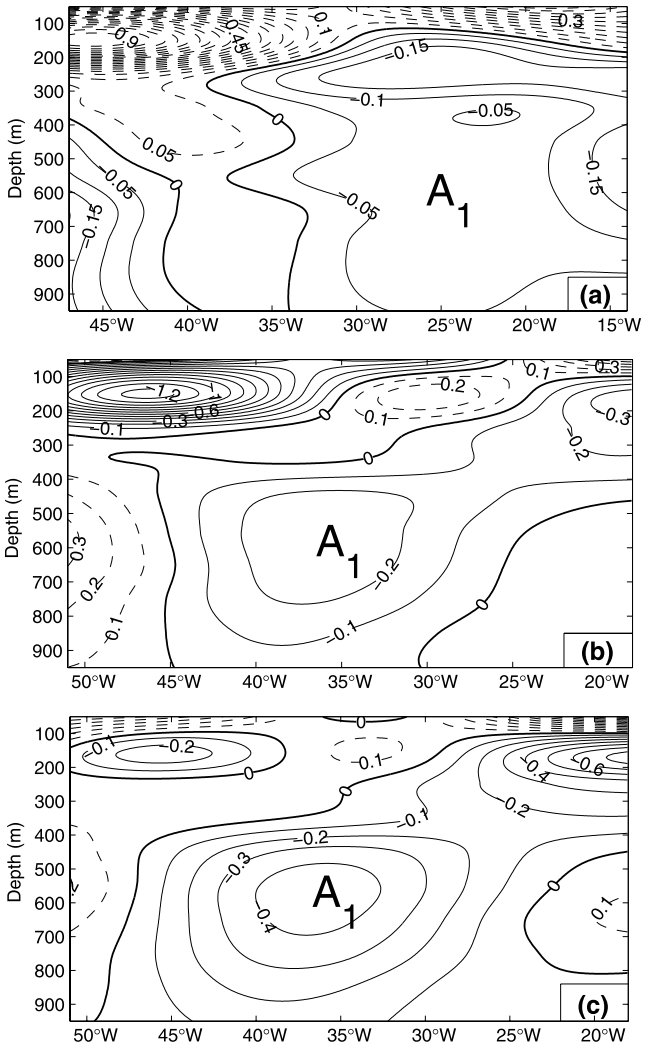

Figure 10. Zonal cross-sections of the annual component of the temperature anomaly (°C): (a) along 6°N in June 2004, (b) along 11°N in October 2004, and (c) along 16°N in October 2004. Here the temperature perturbation A_1 corresponds to the velocity perturbation A_1 shown in Figure 8.

[66] Therefore the Wentzel-Kramer-Brullouin (WKB) approximation does not seem to be applicable for the analysis of the annual signal.

[67] Temperature wakes of the annual Rossby wave are clearly observed at 950-m depth (Figure 9) and shallower. Negative temperature anomalies correspond to cyclonic vorticity of the mid-depth currents and vice versa. Both positive and negative anomalies move northwestward and westward with speeds of about 7–10 cm/s. However, annual temperature anomalies can be driven not only by the annual Rossby wave. Our estimations show that the horizontal heat flux caused by annual mean circulation at 1000 m has the same value as the one induced by the annual Rossby wave.

[68] The vertical thermal structure of the annual Rossby wave is shown in Figure 10. The annual temperature anomaly at 950-m depth oscillates in antiphase, with the annual stream function computed at a 1000-m depth. The weak temperature response observed immediately after excitation of the perturbation A_1 in June 2004 (Figure 10a) becomes stronger in October 2004 (Figures 10b and 10c) when the wave has reached the 11°N–16°N latitude band.

[69] Wave wakes in temperature have explicit maximum at 500–600 m (Figure 10). However, a wave structure shallower than 200 m is not clear because the wave baroclinic signal is masked by temperature anomalies propagating eastward, probably with the North Equatorial Counter Current. Although over complex bottom topography, as in the tropical North Atlantic Ocean, the governing equations for Rossby wave dynamics are not separable so that Rossby waves can jump from one vertical mode to another, sometimes it is useful to interpret the vertical structure of the Rossby waves using the classical baroclinic Rossby modes [*Pedlosky*, 1987; *Rhines*, 2004].

[70] The climatic temperature and salinity [*Levitus et al.*, 1998] were used to compute the standard normal modes $\Phi_l(z)$ ($l = 1, \ldots, L$) and to represent the buoyancy $b = -g\rho/\rho_0$ as

$$b(\lambda, \varphi, z, t) = -N^2(z) \sum_{l=1}^{L} \Lambda_l(\lambda, \varphi, t)\Phi_l(z), \qquad (17)$$

where ρ and ρ_0 are the water density and a reference density, respectively; g is the gravitational acceleration; $N^2 = -(g/\rho_0)\frac{d\bar{\rho}_0}{dz}$ is the Brunt-Vaisälä frequency computed from the mean density profile $\bar{\rho}_0$.

[71] The first three baroclinic modes computed at 16°N, 38°W are demonstrated in Figure 11a. It is clear that to reproduce the vertical temperature structure with a maximum at 500–600 m (Figure 10c), the second baroclinic mode alone or in combination with other modes should be taken in the decomposition (17). Figure 11b shows several possible combinations composed from three baroclinic modes. The second baroclinic mode explicitly dominates in any combination, which is the best fit to the vertical temperature distribution shown in Figure 10b. Although a different combination of the baroclinic modes is responsible for adjustment in different areas of the eastern subbasin, the second baroclinic mode (the leading mode) always plays a dominant role. This effect seems to be true for a shallow thermocline and can be explained similarly to the work of *Phylander and Pacanowski* [1980].

6.2. Effects of Bottom Topography

[72] Dynamics of the annual Rossby wave excited in the eastern subbasin are strongly influenced by the variable topography. That results in (1) the northwestward propagation of the wave and (2) that propagation speed tries to be oriented along isobaths, until the wave reaches the region between 10° and 20°N where it crosses the MAR. *Herrmann and Krauss* [1989] found similar behavior for the first baroclinic Rossby waves in a nonlinear quasi-geostrophic model on the β plane, with realistic topography and coastal geometry of the North Atlantic in the area of 10°–50°N, 10°–80°W.

[73] Another effect of topography on a Rossby wave train was first investigated by *Barnier* [1988]. He pointed out that a meridional ridge in the simplified topography of his nonlinear quasi-geostrophic model acts as a barrier to the westward propagation of waves generated at the eastern boundary. Coupling of the barotropic and baroclinic parts over topography generates new baroclinic Rossby waves at a meridional ridge [*Wang and Koblinsky*, 1994].

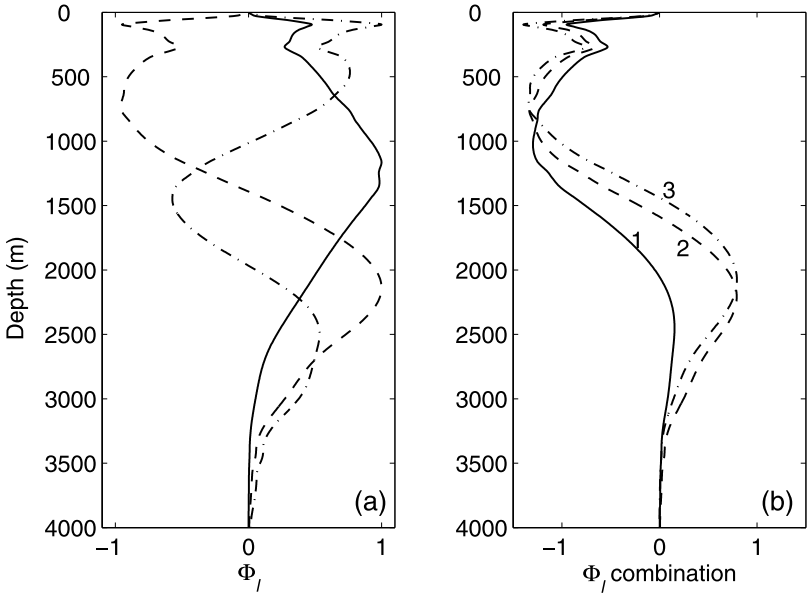

Figure 11. Mode decomposition for the buoyancy: (a) first (solid curve), second (dashed curve), and third (dotted-dashed curve) baroclinic Rossby modes computed in the eastern subbasin (16°N, 38°W) using the World Ocean Atlas (T,S) data [*Levitus et al.*, 1998]. The Rossby radius of deformation for the first, the second, and the third modes is 67.3, 50.9, and 41.8 km, respectively. (b) Combinations of several baroclinic modes: (1) $1.0 \cdot \Phi_1 + 0.5 \cdot \Phi_2$; (2) $0.5 \cdot \Phi_1 + 1.0 \cdot \Phi_2$; and (3) $0.3 \cdot \Phi_1 + 1.0 \cdot \Phi_2 - 0.3 \cdot \Phi_3$.

[74] Our computations do not demonstrate a wave generation at the MAR. The annual wave crossing MAR south of 15°N only strongly disperses and dissipates (Figures 8c and 8d). However, we should understand that a wave transformation over the MAR is probably a dynamical process with a variability of 1 month and shorter. Clearly, such a process might not be extracted from the Argo float data.

6.3. Mechanisms for Wave Generation

[75] In the tropical North Atlantic Ocean, the annual Rossby waves may be generated within the interior of the ocean because of direct wind-forcing and along the eastern boundary because of either along-shore wind fluctuations or equatorially forced coastal Kelvin waves [*Krauss and Wuebber*, 1982; *Chang et al.*, 2005]. It is difficult to separate contributions from all these mechanisms even when using long observation series and high-resolution numerical model results. However, some useful conclusions about the contributions from the physical mechanisms involved in the wave generation may be done, analyzing the mean kinetic energy (KE) of annual NCEP/NCAR wind ($\langle E_i \rangle$), the mean KE of the annual mid-depth currents ($\langle e_i \rangle$), the correlations between the annual wind stress [$\boldsymbol{\tau} = (\tau_1, \tau_2)$] and annual mid-depth current velocity [$\mathbf{u} = (u_1, u_2)$]

$$R_{ii}(t) = \langle u_i \tau_i \rangle \cdot \left\langle u_i^2 \right\rangle^{-1/2} \cdot \left\langle \tau_i^2 \right\rangle^{-1/2}, \tag{18}$$

and between the annual wind stress curl [$\mathrm{rot}_z(\boldsymbol{\tau})$] and ψ_1

$$\hat{R}_{11}(t+\delta t) = \langle \mathrm{rot}_z[\boldsymbol{\tau}(t)] \cdot \psi_1(t+\delta t) \rangle \cdot \left\langle \mathrm{rot}_z[\boldsymbol{\tau}(t)]^2 \right\rangle^{-1/2} \cdot \langle \psi_1^2(t+\delta t) \rangle^{-1/2}, \tag{19}$$

where δt is the time lag, $\langle \ldots \rangle = G(\ldots)/G(1)$ is averaging over an area of interest S (the western or eastern subbasin), $G(\ldots) = \iint_S \ldots d\lambda d\varphi$. Since the mid-depth currents were reconstructed from bimonthly averaged float velocities, the correlations with the time lag $\delta t \leq 1$ month should contribute to "zero" lag correlation functions $R_{ii}(t)$ and $\hat{R}_{11}(t)$.

6.3.1. Western Subbasin

[76] Appropriate energetic and correlation characteristics averaged over the western subbasin are shown in Figure 12. Comparing Figures 12a with 12b, we find that the wind and current KEs ($\langle E_i \rangle$, $\langle e_i \rangle$) oscillate out of phase. The phase shift equals to 3 and 4 months for the zonal and meridional components, respectively. Therefore the maximal current KE corresponds to the minimal kinetic energy of wind and vice versa. Ratio of max KE/min KE for the mid-depth currents equals approximately to 5.10 and 3.70 for the zonal and meridional components, respectively.

[77] Figure 12c shows that maximum correlations ($R_{11} \approx R_{22} \approx 0.60$) between the annual wind stress and current velocity are reached in September–October 2004 and March–April 2005 when the KE of mid-depth currents becomes minimal (compare Figure 12b with 12c). Minimum correlations (even with negative values for R_{11}) correspond to maximum KEs of the currents.

[78] Zero-lag correlations between $\mathrm{rot}_z(\boldsymbol{\tau})$ and ψ_1 are maximum ($\hat{R}_{11} \approx 0.60$) in April 2004, October 2004, and April 2005 (Figure 12d) when the mean KE of the mid-depth currents varies between 0.1 and 0.5 $\mathrm{cm}^2/\mathrm{s}^2$ (Figure 12b). This KE is considerably less than the squared amplitude of the annual Rossby wave, which is about 1.1 $\mathrm{cm}^2/\mathrm{s}^2$.

[79] Large correlations between $\mathrm{rot}_z(\boldsymbol{\tau})$ and ψ_1 ($\hat{R}_{11} \approx 0.49$) are observed at the time lag of 3 months from July 2004

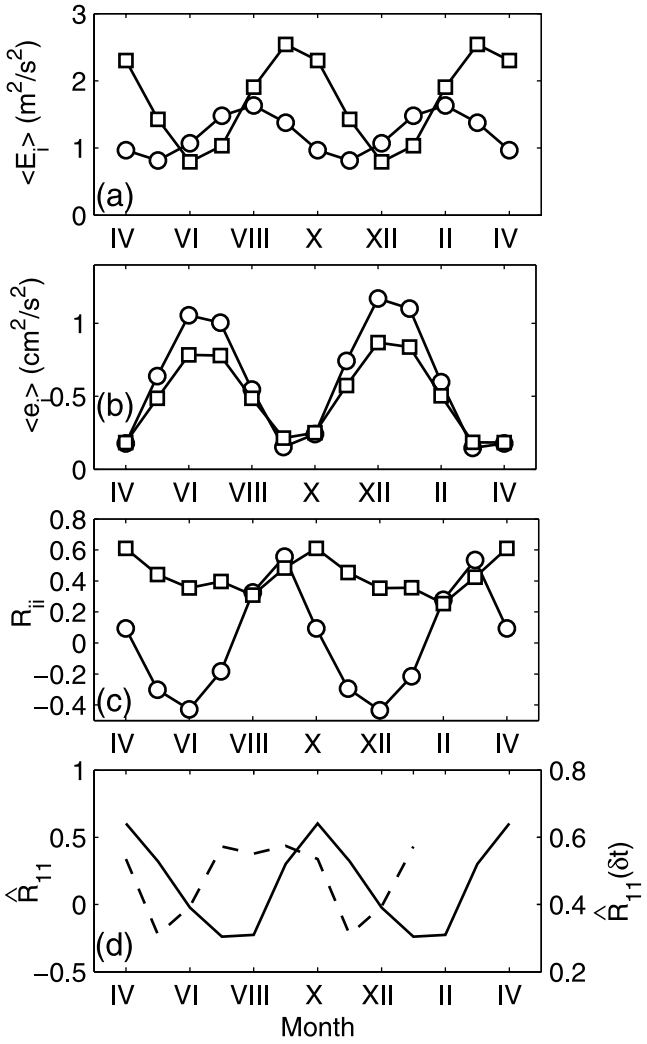

Figure 12. Characteristics of the annual oscillation in the western subbasin: (a) the mean wind KE, (b) the mean KE of mid-depth currents, (c) correlations between wind stress and currents, and (d) correlations between the wind stress curl and the stream function of mid-depth currents. Here circles and squares represent zonal and meridional components. Solid and dashed curves in Figure 12d correspond to 0- and 3-month lags, respectively.

to October 2004 (Figure 12d). Taking into account the periodicity of the stream function ψ_1 and the 3-month lag in the generation of the mid-depth currents, May–June 2004 and November–December 2004 seem to be time periods when the wind Ekman pumping dominates these currents. No significant correlations between $\mathrm{rot}_z(\boldsymbol{\tau})$ and ψ_1 are observed for $\delta t > 3$ months. These results indicate that the standing Rossby wave observed in the western subbasin was likely excited by the wind-driven Ekman pumping.

6.3.2. Eastern Subbasin

[80] Comparing Figure 13a with 13b, we find that the wind KE and KE of the mid-depth currents for both zonal and meridional components oscillate exactly in antiphase, that is, minimum KE of currents corresponds to maximum wind KE and vice versa. Although the ratio of max $\langle E_1 \rangle$/ max $\langle E_2 \rangle$ is only about 0.46, the same ratio estimated for the mid-depth currents is about 2.88.

[81] Correlations between the wind stress and current velocity are maximum ($R_{11} = 0.81$; $R_{22} = 0.52$) in August 2004 and February 2005 (Figure 13c) when the wind KE is also maximum. However, KE of the mid-depth currents is low (less than 0.5 cm^2/s^2) for both these time periods. Thus, the probability that the annual Rossby wave is an interference of the barotropic ocean response due to wind and baroclinic oscillations is also low. The barotropic component of the mid-depth circulation seems to be small.

[82] In contrast to R_{ii}, correlations between the wind stress curl and ψ_1 reach the maximum values (max $\hat{R}_{11} \approx 0.72$) in July–August 2004 and January–February 2005

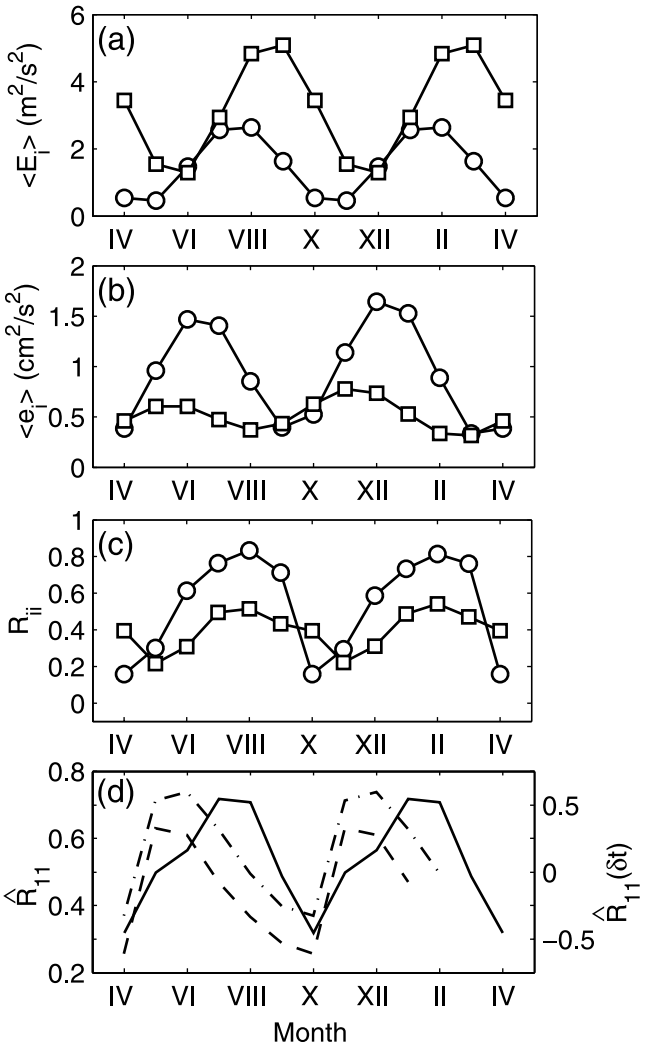

Figure 13. Characteristics of the annual oscillation in the eastern subbasin: (a) the mean wind KE, (b) the mean KE of mid-depth currents, (c) correlations between wind stress and currents, and (d) correlations between the wind stress curl and the stream function of mid-depth currents. Here circles and squares represent zonal and meridional components. Solid, dotted-dashed, and dashed curves in Figure 13d correspond to 0-, 2- and 3-month lags, respectively.

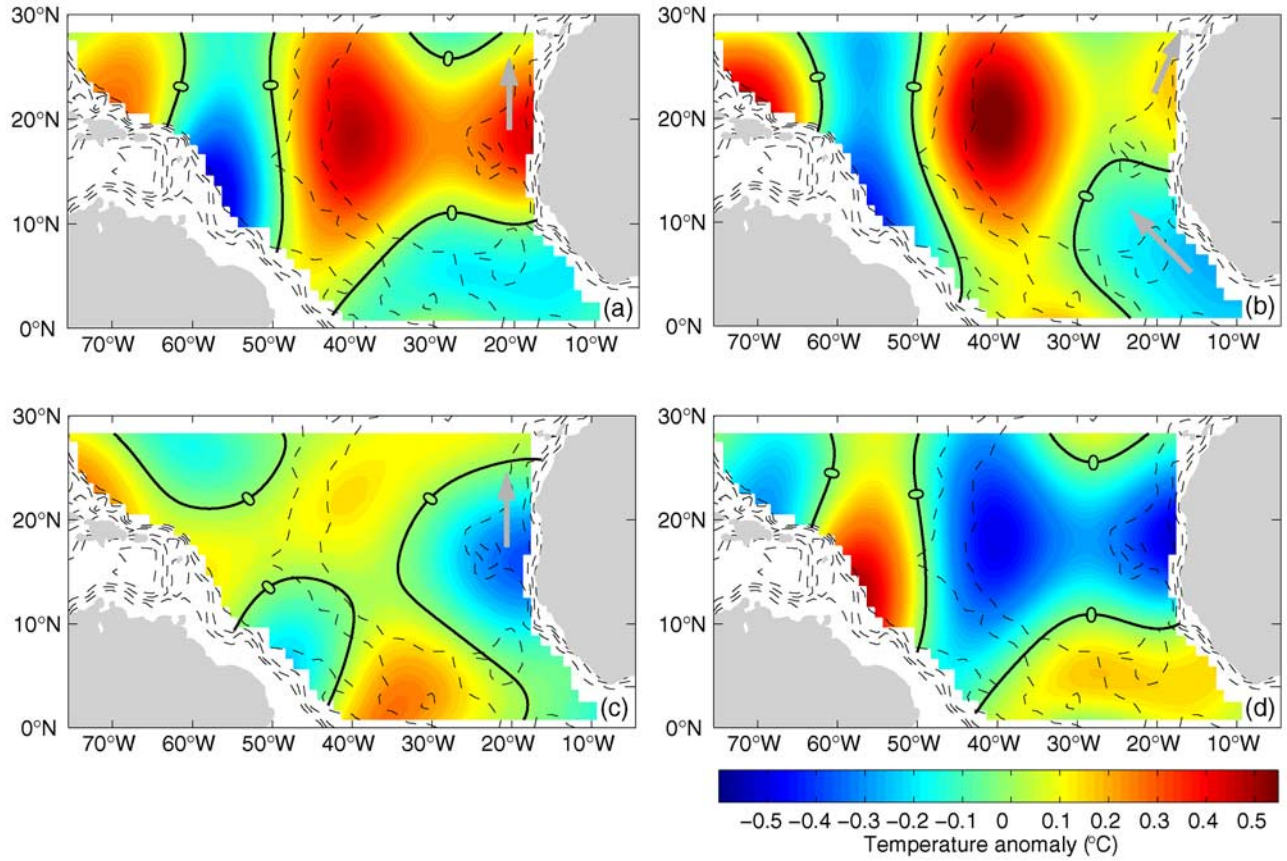

Figure 14. Spatiotemporal structure of annual monthly temperature anomaly at 250-m depth: (a) June 2004, (b) August 2004, (c) October 2004, and (d) December 2004.

(Figure 13d). Peaks of $\hat{R}$ shift to earlier months, reducing their heights if the time lag δt grows (Figure 13d). There are no significant correlations between these characteristics for $\delta t \geq 3$ months (max $\hat{R}_{11} \approx 0.36$). These results do not seem to support the hypothesis about excitation of the annual Rossby wave in the eastern basin by the wind-driven Ekman pumping.

[83] Therefore we suppose that the observed annual Rossby wave may be excited along the eastern boundary because of along-shore wind fluctuations and/or an equatorially forced coastal Kelvin wave. Probably, temperature wakes of such a Kelvin wave (maybe even a beam of waves) are clearly observed in Figure 14. It shows a temperature anomaly propagating along the African coast in the upper ocean layer shallower that 200–250 m and with a speed of about 27–30 cm/s. It is a reasonable assumption that a temperature anomaly is driven by an equatorially forced coastal Kelvin wave.

[84] The annual Rossby wave causes oscillations of the thermocline with an amplitude (A_{ocean}) of about 16 m (estimated from three-dimensional temperature field reconstructed from the Argo float data). The amplitude of such oscillations near the African coast (A_{bond}) is about 26 m, i.e., $A_{\text{ocean}} \sim A_{\text{bond}}$. *Wang et al.* [2001] demonstrated that a similar relationship is only true if the Rossby wave is formed at the ocean boundary. Therefore the annual Rossby wave observed in the eastern subbasin was likely excited by a forcing along the eastern boundary.

7. Semiannual Rossby Waves

7.1. Kinematic Characteristics

[85] The semiannual oscillation of the mid-depth currents appears as a combination of two unstable standing waves (labeled by C_1 and C_2, and D_1 and D_4, respectively, in Figures 15a–15e) with the phases shifted relative to one another approximately by half the period. Decaying, the waves generate shorter free Rossby waves propagating westward and northwestward because of the β effect, bottom topography, and coastline geometry. Wave dynamics at the temporal scales shorter than 2 months were reconstructed using decomposition (8) with the prescribed amplitudes $A_{\omega_2,s}$ and $B_{\omega_2,k}$ and phases $\theta_{\omega_2,s}$ and $\vartheta_{\omega_2,k}$.

[86] One of these waves with the characteristic length scales of about 2160–2500 km is excited in the eastern subbasin (Figure 15b). This wave is unstable and decays in two stages. At the first stage (elliptic instability stage) a corotating anticyclonic eddy pair ($D_1 + D_3$) is generated through a decay of a corotating cyclonic eddy pair ($D_2 + D_4$) (Figures 15b and 15c). Reclosing of vortex isolines while forming a new corotating eddy pair typically indicates excitation of periodical auto-oscillations in hydrodynamic flows (e.g., see *Rabinovich and Trubetskov* [1989]).

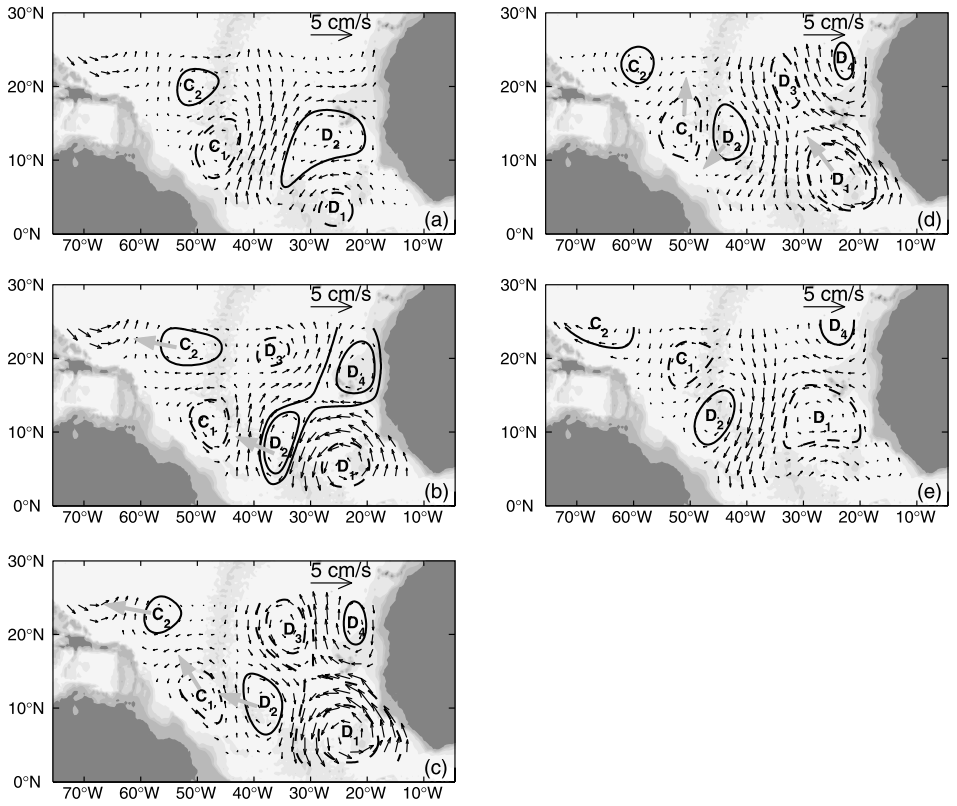

Figure 15. Spatiotemporal structure of the semiannual currents at 1000-m depth in 2004: (a) 15 May, (b) 30 May, (c) 14 June, (d) 29 June, and (e) 13 July 2004. Here the gray arrows show the direction of the Rossby wave propagation.

[87] At the second stage, the corotating anticyclonic eddy pair also decays (Figure 15d), that excites smaller scale perturbations propagating westward (D_2) or northwestward (D_1 and D_4) because of the β effect, bottom topography, and coastline geometry. The propagation speeds for such perturbations are between 5 cm/s and 10 cm/s. They can be identified as free Rossby waves with the characteristic length scale of about 1000 km.

[88] Another wave occupying the western subbasin (labeled as C_1 and C_2 in Figure 15a) is also unstable. Its decay causes the generation of shorter waves propagating northwestward (Figures 15c and 15d). The currents associated with this wave are considerably weaker than in the eastern subbasin.

[89] The wave D_2 crosses the MAR propagating southwestward (Figure 15d). That may be explained by nonlinear interactions between the waves C_1 and D_2 or by reconstruction errors. We have no arguments to support or reject any of these hypotheses.

[90] The semiannual temperature anomalies (wakes of semiannual Rossby waves in temperature) occupy the tropical North Atlantic from the African coast to the coast of South America (Figure 16). A baroclinic signal propagating from the eastern boundary westward and downward is explicitly observed in Figure 16. Fixing two consequent positions of the absolute maximum of the vertical distribution of temperature anomaly (420 m in June 2004 and 680 m in August 2004), we estimated zonal and vertical propagation speed of such a signal as about 13–14 cm/s and $3-5 \times 10^{-3}$ cm/s, respectively. The horizontal structure of the temperature anomaly is demonstrated in Figure 17.

[91] Similarly to annual Rossby waves, the vertical temperature structure of a semiannual wave with a maximum at 650- to 700-m depth may also be approximated by a combination of the first three baroclinic modes (vertical structures of modes are presented in Figure 11). However, since the absolute maximum is deeper than 600 m, the weight of the first baroclinic mode in such a combination should be larger than for the annual Rossby wave.

[92] Only a weak contribution of the westward traveling Rossby wave may be observed in the mid-depth velocity reconstructed at 1000 m (compare Figure 8 with Figure 15). We may explain this fact by the existence of an inflection point in the vertical structure of horizontal velocity corresponding to the temperature anomaly at about 1000 m.

7.2. Mechanisms of Wave Generation

[93] Although the semiannual winds are much weaker than the annual ones, the semiannual mid-depth currents in the eastern subbasin are not less energetic than the annual mid-depth currents (compare Figure 8 with Figure 15). *Li* [1996] found the same phenomenon analyzing *Semtner and Chervin*'s [1992] model output for the equatorial North Atlantic. *Thierry et al.* [2004] assumed that a linear resonance could be involved to explain this phenomenon. We suggest a nonlinear resonance mechanism for the semiannual Rossby wave excitation in both the subbasins.

[94] According to the classical theory [*Pedlosky*, 1987] for long Rossby waves, a linear balance exists between the

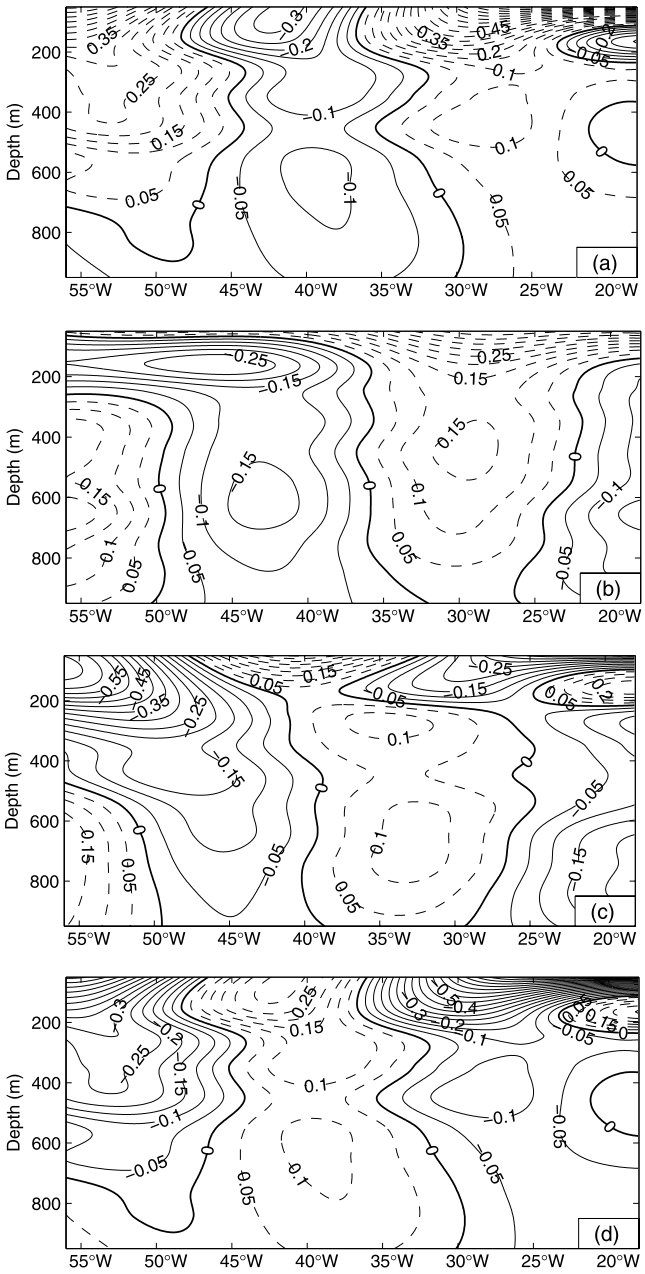

Figure 16. Zonal cross-sections of the semiannual component of monthly temperature anomaly (°C) along 11°N: (a) June 2004, (b) July 2004, (c) August 2004, and (d) September 2004.

acceleration term and the sum of the pressure gradient and the Coriolis force. Although this balance dominates the mid-depth ocean dynamics, a number of numerical studies demonstrate that the deviation to this balance is non-negligible.

[95] *Thierry et al.* [2004] pointed out that such a deviation might reach up to 16% at the mid-depths of tropical Atlantic Ocean between 13°S and 13°N. *Gerdes and Wübber* [1991] studied the seasonal variability of the North Atlantic using both a primitive equation model and a linear quasi-geostrophic model. They found that the spatial variability of the density distribution, modal interactions, and the finite amplitude aspects of the bottom topography are the most important factors for generating Rossby waves. *Cox* [1987] produced evidence that low-frequency oscillations (Rossby waves) in the North Atlantic are excited during adjustment, even with steady forcing.

[96] The discussion above shows that (1) low-frequency oscillations in the North Atlantic may be excited at frequency[s], which differ from external forcing frequency, and (2) ocean environment parameters such as density and bottom topography determine frequency[s] of these oscillations. According to the general theory of nonlinear oscillations (e.g., see *Landa* [1996]), such features indicate the wave excitation by a nonlinear resonance mechanism. In our opinion, a nonlinear resonance mechanism[s] may also be responsible for the excitation of the semiannual standing Rossby waves by wind.

7.2.1. Western Subbasin

[97] The KE of semiannual wind $\langle \tilde{e}_i \rangle$ and KE of semiannual mid-depth currents $\langle \tilde{e}_i \rangle$ in the western subbasin oscillate exactly in antiphase: weakest currents ($\langle \tilde{e}_1 \rangle \approx \langle \tilde{e}_2 \rangle \approx 0.1$ cm^2/s^2) correspond to strongest winds ($\langle \tilde{E}_1 \rangle \approx 2$ m^2/s^2, $\langle \tilde{E}_2 \rangle \approx 0.5$ m^2/s^2) and vice versa (Figures 18a and 18b). Correlations between the semiannual wind stress and semiannual current velocity (estimated by appropriate correlation function $\tilde{r}_{ii}$) are small, $\tilde{R}_{11} \approx 0.05$ and $\tilde{R}_{22} \approx 0.18$ (Figure 18c).

[98] Another possible mechanism for wave excitation in the western basin is the generation of the semiannual currents by both the annual mean wind stress and the annual wind stress. In contrast to the annual currents, our computations demonstrate high correlations between the annual mean wind stress and semiannual current velocity in July–August 2004 and January–February 2005 when maximum values of appropriate correlation function for the meridional components ($\bar{r}_{22}$) are 0.59 (Figure 18d). The meridional KE of the semiannual currents is also maximum for these time periods. This indicates possible excitation of the semiannual oscillation of the mid-depth currents by the meridional component of average annual wind stress.

[99] High correlations between the annual wind stress and semiannual current velocity observed in October 2004 and February 2005 (Figure 18e) (appropriate correlations function $\tilde{r}_{22}$ reaches 0.6) indicate that the meridional component of annual wind stress may also contribute to the excitation of semiannual Rossby wave. The zonal wind stress does not seem to be a significant contributor to wave generation because the maximum values of $\bar{r}_{11}$ and $\tilde{r}_{11}$ (Figures 18d and 18e) correspond to minimum values of $\tilde{e}_1$ (Figure 18b).

[100] Thus, the semiannual standing waves in the western subbasin may be explained in terms of interference between an ocean response to Ekman pumping and oscillations excited by meridional wind stress with annual and longer timescales through a nonlinear resonance mechanism. The wind-currents resonance interactions should be important in the fall-winter period and less significant in summer. The wind-driven Ekman pumping seems to be effective year round. However, we cannot exclude that this pumping only masks nonlinear resonance effects. The last hypothesis needs to be examined using high-resolution primitive equation models.

7.2.2. Eastern Subbasin

[101] In the eastern subbasin, the kinetic energies $\langle \tilde{E}_1 \rangle$ ($\langle \tilde{E}_2 \rangle$) and $\langle \tilde{e}_1 \rangle$ ($\langle \tilde{e}_2 \rangle$) oscillate in phase (antiphase) (Figures 19a

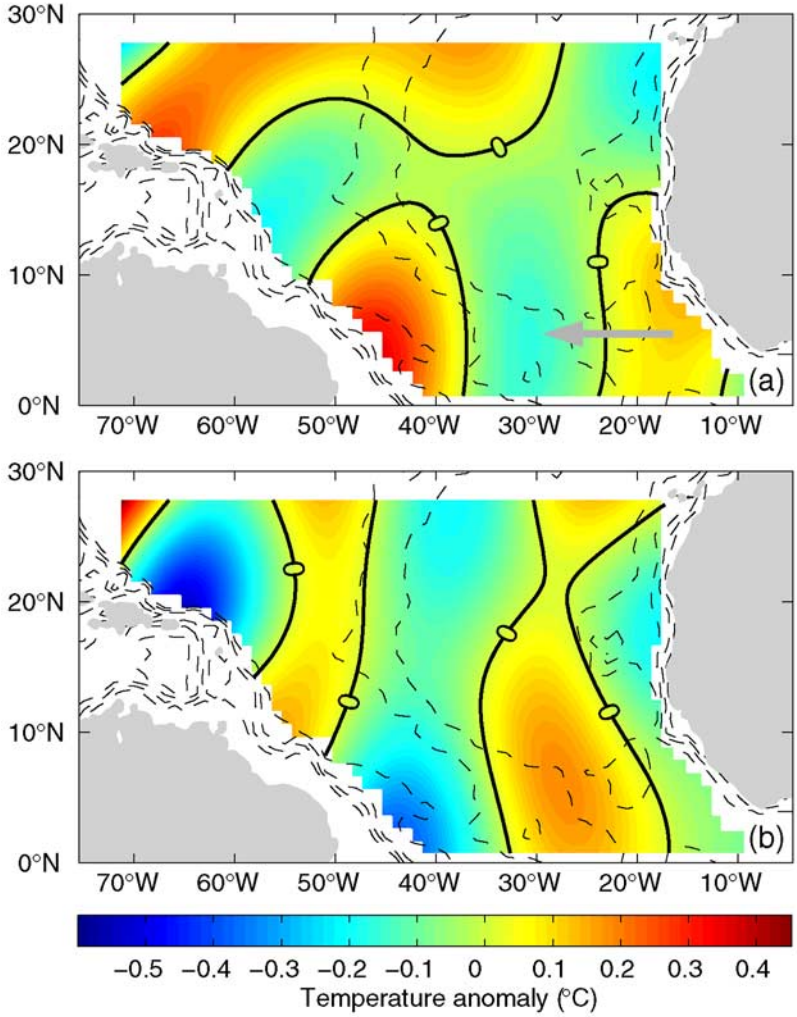

Figure 17. Spatiotemporal structure of semiannual temperature anomaly at 550-m depth: (a) 15 May and (b) 29 June 2004. Here the gray arrow shows the direction of the propagation of the positive temperature anomaly.

and 19b). The meridional semiannual wind stress and mid-depth currents weakly correlate ($\tilde{R}_{22} \leq 0.25$) but correlations between the zonal wind stress and current velocity are quite high ($R_{11} \approx 0.5$) in May 2004, August 2004, October 2004, and February 2005 (Figure 19c), when the KE $\langle e_1 \rangle$ reaches the maximum values about 0.6 cm^2/s^2 (Figure 19b). Therefore we may propose that the zonal semiannual wind stress may excite the semiannual wave in the eastern subbasin.

[102] Maximum correlations ($\bar{r}_{22} \approx 0.8$) in July 2004 and January 2005 (Figure 19d) correspond to minimum values of kinetic energy $\langle \tilde{e}_2 \rangle$ (Figure 19b). That shows a weak contribution of wind stress to the meridional flows. Zonal annual mean wind stress weakly correlates with the zonal semiannual current velocity ($\bar{r}_{11} \leq 0.25$). Therefore we can exclude the annual mean wind stress as a possible reason of Rossby wave excitation in the eastern subbasin.

[103] However, correlations between zonal annual wind stress and zonal semiannual current velocity are not small in August 2004 and November–December 2004 (Figure 19e) when the appropriate correlation function $\tilde{r}_{11}$ reaches 0.75. In contrast to the zonal component, the meridional annual wind stress may not probably excite the meridional semiannual current velocity because the correlation function $\tilde{r}_{22}$ is small when $\langle \tilde{e}_2 \rangle$ is maximum (compare Figure 19b with 19e).

[104] The above results support a hypothesis that the semiannual quasi-standing Rossby waves in the eastern subbasin may be excited by the wind-driven Ekman pumping, the zonal wind stress with the annual and semiannual periods through nonlinear and linear resonance mechanisms, respectively. Unfortunately, contributions of each mechanism cannot be estimated using only Argo float data because bimonthly averaging is applied to reconstruct the mid-depth currents, and dissipative processes in the eastern subbasin are not clear.

8. Additional Analysis of Float Tracks From May 2005 Through May 2006

[105] To understand a realism of the obtained results and estimate their robustness relative to observational sampling, we have reconstructed the annual and semiannual currents

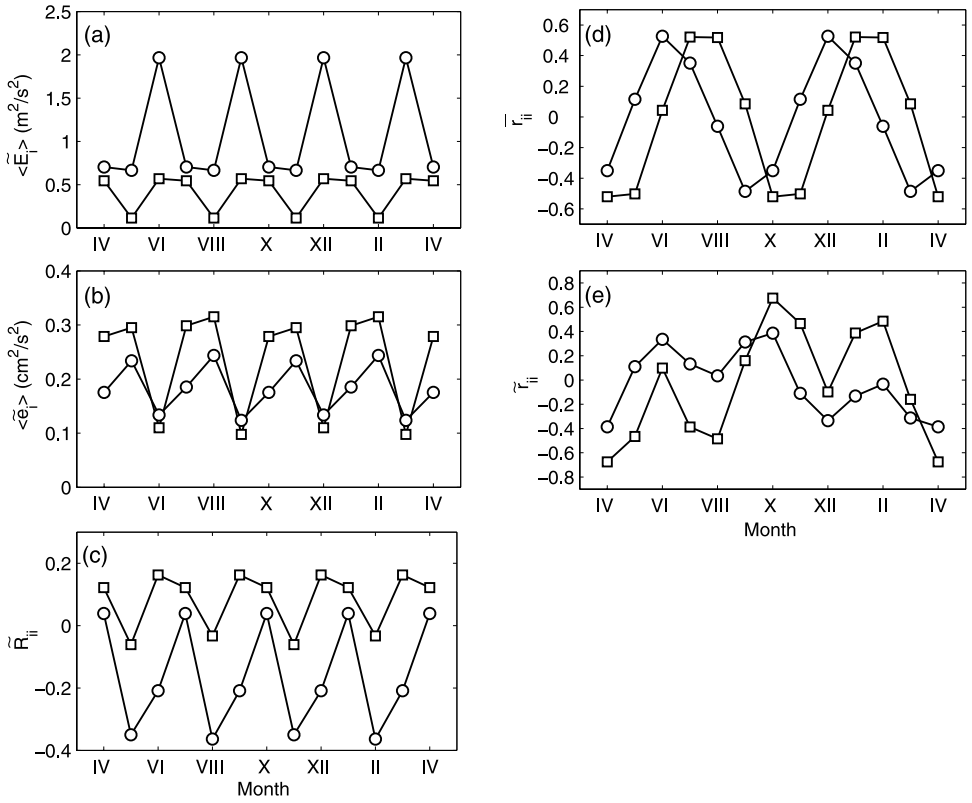

Figure 18. Characteristics of the semiannual oscillation in the western subbasin: (a) the mean wind KE; (b) the mean KE of mid-depth currents; (c) correlations between wind stress and currents; (d) correlations between semiannual currents at 1000-m depth and annual mean wind stress; and (e) correlations between semiannual currents at 1000 m and annual wind stress. Here circles and squares represent zonal and meridional components, respectively.

from float tracks detected between March 2004 and May 2006, using the same numerical technique as in section 3.

[106] Circulation snapshots were additionally reconstructed for 11 overlapping intervals created as May–June 2005; June–July 2005; . . .; and April–May 2006. Together with 14 snapshots reconstructed from March 2004–May 2005 float data, we obtained 25 snapshots for the spectral analysis.

[107] A visual inspection of the snapshots shows explicit recurrence of circulation dynamics within the 2-year period. As an example, we compare the mid-depth currents reconstructed in August–September 2004 and August–September 2005 (Figures 20a and 20b). Current structures are similar, and the root mean square difference between the structures is less than 28%.

[108] We applied the spectral decomposition similar to equation (6), but with the addition of biannual harmonic, to 25 circulation snapshots and selected the annual and semiannual signals. Then, these signals were compared with those reconstructed from March 2004–May 2005 float data only.

[109] This comparison demonstrates no new specificities or dynamical processes in both the subbasins. Comparing Figure 8b (Figure 8c) with Figure 21a (Figure 21b) we can identify the same dynamical process as the one detected from March 2004–May 2005 float data. The same annual Rossby wave is generated in the western subbasin (labeled by B_1), and the same dynamical process (the wave decay with radiation of a free Rossby wave) is uniquely identified in both these figures. The propagating Rossby wave with the annual period (labeled by A_1) is clearly observed in the eastern subbasin. It propagates northwestward and crosses MAR south of 15°N (compare Figure 8c with Figure 21b). The magnitudes of propagation speeds (c_p) and wave characteristic length scales (L_1, L_2) as they are defined in section 6 weakly depend on the length of observational sampling. These wave characteristics computed from March 2004–May 2005 and March 2004–May 2006 float data are given in Table 1. The difference between the kinematic characteristics computed for different data is not essential.

[110] Computations using the March 2004–May 2006 float data reproduce such an important dynamical effect as reclosing of vortex isolines between corotating eddies, which are components of the semiannual standing Rossby wave originating in the eastern subbasin. This effect is clearly demonstrated in Figures 15b, 15c, 22a, and 22b.

[111] The mean kinetic energy of mid-depth currents with the annual and semiannual periods is also nonsensitive to observational sampling. The ratios of the mean kinetic energy of the annual currents to the mean kinetic energy of the semiannual currents calculated for the western (eastern) subbasin were about 2.89 (1.61) and 2.55 (1.56) for March 2004–May 2005 and March 2004–May 2006 float data, respectively. The mean kinetic energy of the

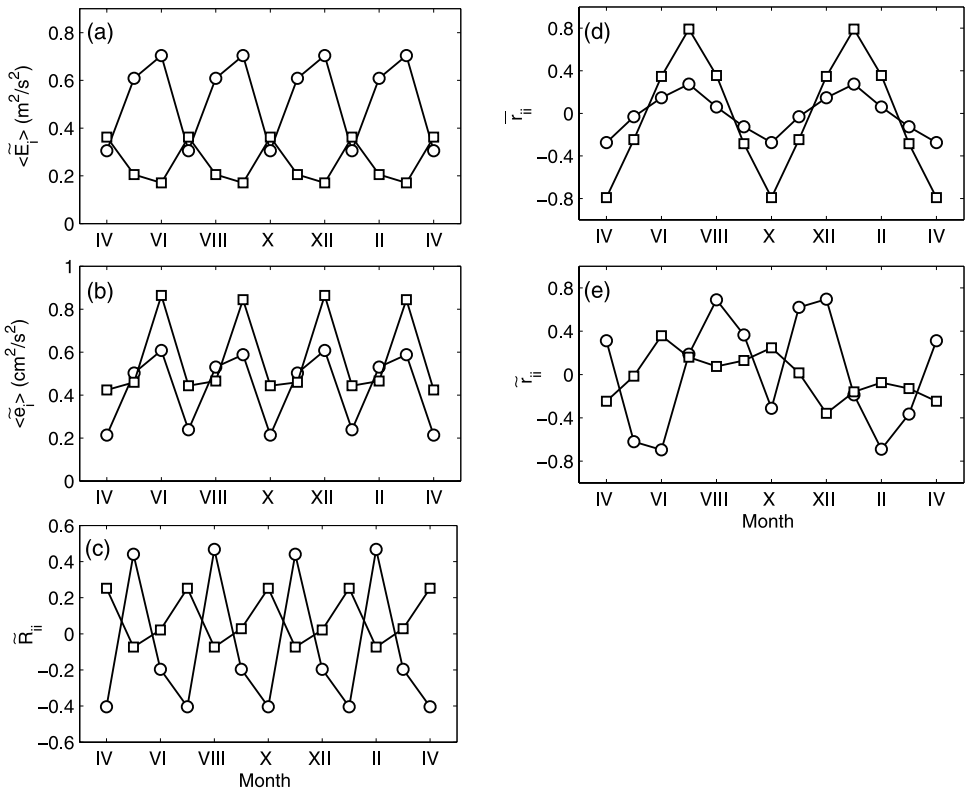

Figure 19. Characteristics of the semiannual oscillation in the eastern subbasin: (a) the mean wind KE; (b) the mean KE of mid-depth currents; (c) correlations between wind stress and currents; (d) correlations between semiannual currents at 1000-m depth and annual mean wind stress; and (e) correlations between semiannual currents at 1000-m depth and annual wind stress. Here circles and squares represent zonal and meridional components, respectively.

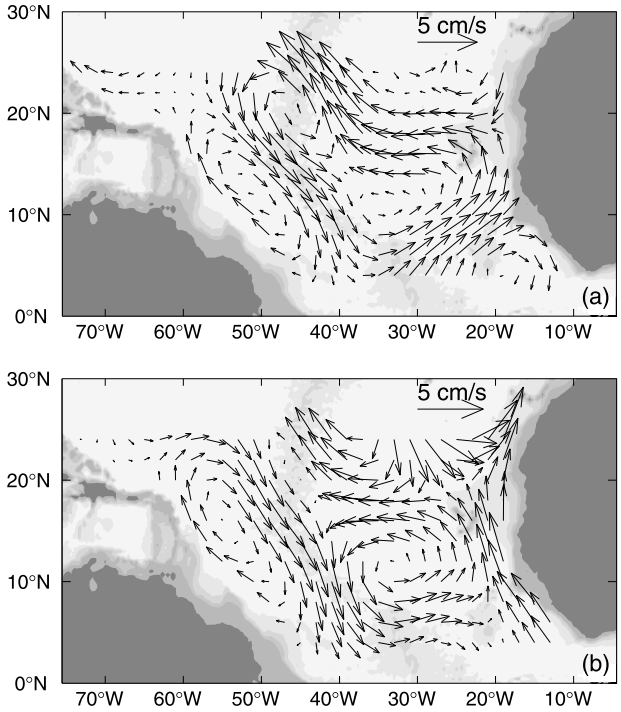

Figure 20. Mid-depth currents reconstructed (a) from August–September 2004 Argo float data and (b) from September–October 2005 Argo float data.

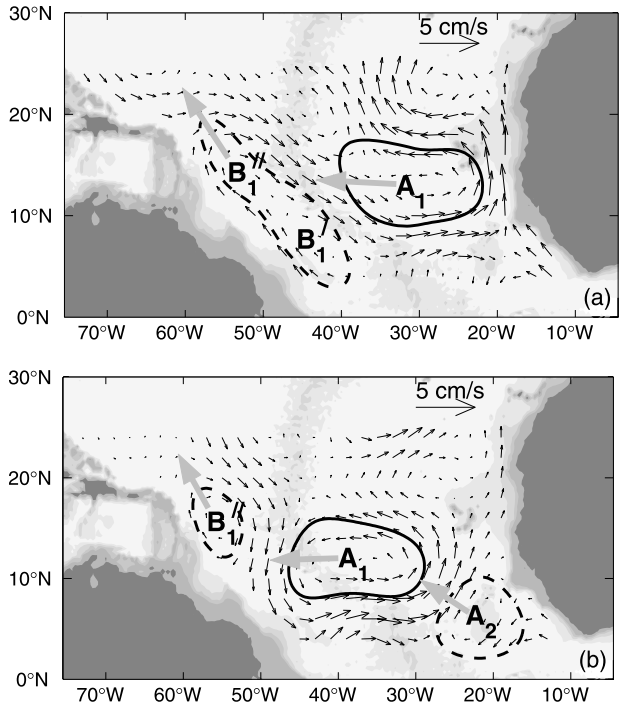

Figure 21. Spatiotemporal structure of the annual currents reconstructed from March 2004–May 2006 Argo float data: (a) July–August and (b) September–October. Notations are the same as in Figure 8.

Table 1. Kinematic Characteristics of the Annual Rossby Wave A_1 Propagating in the Eastern Subbasin (Notations are Explained in Section 6)

	March 2004–May 2005 Float Data			March 2004–May 2006 Float Data		
Latitude	c_p, cm/s	L_1, km	L_2, km	c_p, cm/s	L_1, km	L_2, km
5°N	12	1800	1200	12	1900	1000
8°N	16	2500	1400	12	2100	1100
11°N	14	2200	1400	11	1900	1100
13°N	11	2100	1500	10	2300	1500

annual (semiannual) signal decreased approximately only on 20%–25% (10%–15%) with increasing of observation sampling. Such changes are due to a reconstruction error (see section 3) and redistributing of the kinetic energy between the biannual, annual, and semiannual harmonics of the reconstructed signal. But no changes of the spatial structure of this signal are observed.

[112] The results discussed above (1) uniquely indicate robustness of the reconstructed annual and semiannual signals to observation sampling and (2) demonstrate that, probably, they are the seasonal ocean response to wind-forcing and other dynamical factors but not a random event caused by abnormal wind features for March 2004–May 2005.

9. Conclusions

[113] Satellite observations (altimetry, chlorophyll, and SST) and numerical high-resolution models show high activity of Rossby and Kelvin waves in the tropical North Atlantic. However, support for these waves from in situ observations is quite poor. In this paper, the wind-forced basin-scale response of the tropical North Atlantic between 4° and 24°N is studied from the Argo float tracks at 1000-m depth and the float temperature profiles from the ocean surface to 950-m depth.

[114] Since the climatological annual or seasonal cycle may not be extracted from such a short sampling, we have reconstructed a signal containing both the annual and semiannual oscillations within a 14-month time period. The signal frequency was a priori given, and only a phase of the signal is extracted from the data. However, the reconstructed seasonal ocean response to wind-forcing and other dynamical factors does not seem to be a random event caused by abnormal wind features for March 2004–May 2005. The preliminary analysis of the Argo float tracks for 2005–2006 provided in section 8 supports this conclusion.

[115] Below we list a number of physical and methodological results obtained in the present study.

[116] (1) Capability of the Argo float data is presented in analyzing the basin-scale ocean variability without involving numerical model results. The methodology presented in section 3 leads to a robust solution. A priori knowledge may be used to formulate constrains to improve the reconstruction accuracy.

[117] (2) Although the westward-propagating perturbations were early detected at the ocean surface in the tropical North Atlantic from different satellite databases (altimetry, color, and SST) and identified as the baroclinic Rossby waves by a number of investigators, the present analysis gives additional information about the three-dimensional structure of Rossby waves and mechanisms of their excitation.

[118] (3) The baroclinic Rossby wave (defined as a combination of several baroclinic modes with dominant contribution of the second mode) with the annual period and characteristic length scales of 1500–2500 km is detected in the eastern subbasin of the tropical North Atlantic. This wave is probably generated at the eastern boundary because of along-shore wind fluctuations and equatorially forced coastal Kelvin waves. The Rossby wave propagation is strongly controlled by the bottom topography, coastline geometry, and the β effect. This results in propagation speeds varying both in magnitude (between 7 and 14 cm/s) and in direction (between northwestward and westward).

[119] (4) The annual and semiannual unstable standing Rossby waves are detected in both the western and eastern subbasins. The wind-driven Ekman pumping seems to be responsible for the standing wave generation in both the subbasins. However, the correlation analysis shows that the semiannual waves may be excited by average annual wind stress and stresses with the annual and semiannual periods. That suggests the existence of nonlinear and linear mechanisms for wave excitation. Shorter free Rossby waves are generated during the decay of the annual and semiannual

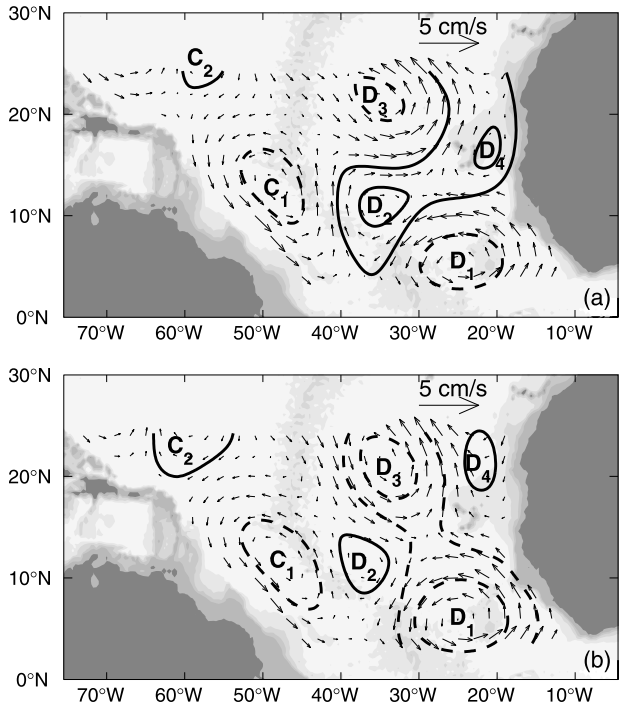

Figure 22. Spatiotemporal structure of the semiannual currents reconstructed from March 2004–May 2006 Argo gloat data: (a) May 30th and (b) June 14th. Notations are the same as in Figure 15.

standing waves. The free Rossby waves propagate northwestward or westward with speeds less than 10 cm/s.

[120] (5) Although in scientific literature there is an opinion (e.g., *Herrmann and Krauss* [1989]) that mesoscale eddies are much more energetic than the Rossby waves in the tropical Atlantic and, therefore, the detailed structure of Rossby waves may be of secondary importance, our computations show that long Rossby waves should affect the southern boundary of the subtropical gyre that may lead to the basin-scale oscillations of the gyre and strong variability of all major pathways in the North Atlantic. Such processes should have an explicit climatic response on Meridional Overturning Circulation at decadal timescales. Evidence for such a mechanism will be published in a separate paper.

Appendix A: Correction of Upper Ocean Current Drifting Effects

[121] To correct position errors for floats due to the vertical shears, a simple procedure was used. *Park et al.* [2005] have assumed that a surface Argo float trajectory consists of large-scale drift, inertial motion, and measurement noise. For temporal scales longer than 2 months, the inertial motions may be considered as spatially uncorrelated "noise" and effectively removed by the OSD.

[122] Systematic float shifts caused by large-scale currents in upper ocean layer were deducted in the following manner. A location of the pth float $\hat{\mathbf{x}}_p$ at the parking depth H_p^0 is specified by the deduction of the "effective" displacement from a location of the same float $\mathbf{x}_p$ after ascending or before descending to the parking depth:

$$\hat{\mathbf{x}}_p = \mathbf{x}_p - \int_{t_p}^{t'_p} \mathbf{U}(wt)\mathrm{d}t, \tag{A1}$$

where $\delta t = t_p - t'_p$ is the ascending/descending time, w is a velocity of ascending or descending.

[123] A phenomenological model is used for $\mathbf{U}_p$:

$$\mathbf{U}_p = \begin{cases} \mathbf{U}_p^{\mathrm{surf}} \exp(-\sigma_p z), & z \le \hat{H}_p \\ \hat{\mathbf{U}}_p, & z > \hat{H}_p \end{cases} \tag{A2}$$

where $\mathbf{U}_p^{\mathrm{surf}}$ and $\hat{\mathbf{U}}_p$ are the surface and mid-depth velocities estimated from the surface and subsurface tracks of the pth float, respectively, $\hat{H}$ is the low boundary of the oceanic thermohaline estimated from temperature profile of the same float, $\sigma_p = -1/(2 \cdot \hat{H}_p) \log(\hat{\mathbf{U}}^2/\bar{\mathbf{U}}^2)$.

[124] For Argo floats launched in the area of interest, we have estimated

$$\mathbf{U}^{\mathrm{surf}} \approx 15 - 20 \text{ cm/s}, \ \hat{\mathbf{U}} \approx 5 - 10 \text{ cm/s}, \ \hat{H} \approx 300 \text{ m}, \quad \delta t = 10 \text{ hours}. \tag{A3}$$

[125] Substituting values (A3) into equations (A1) and (A2) yields that, on average, the position error for the Argo float launched in the area of interest should be less than 6 km. That results in the systematic drift for floats less than 0.6 cm/s. Therefore although the position error of each float was corrected by the method described above, in our opinion the upper ocean drifting effects do not contribute too much to the reconstruction error.

Appendix B: Computation of Basis and Harmonic Functions

[126] The area of interest Ω_1 is bounded by four segments: $\hat{\Gamma}_1$, $\hat{\Gamma}_2$, $\hat{\Gamma}_3$, and $\hat{\Gamma}_4$ (Figure B1a). Following the works of *Eremeev et al.* [1992] and *Ivanov et al.* [2001], there should be no flow across any rigid segment, i.e., across $\hat{\Gamma}_1$ and $\hat{\Gamma}_3$. Boundary conditions for $\hat{\mathbf{U}}$ at open-boundary segments $\hat{\Gamma}_2$ and $\hat{\Gamma}_4$ are, in general, unknown.

[127] To overcome this difficulty, *Chu et al.* [2003] suggested reconstructing $\hat{\mathbf{U}}$ in an extended domain Ω'_1 embedding Ω_1 and applying approximate conditions at an open boundary of Ω'_1. Since reconstruction errors caused by inaccuracy of open-boundary conditions quickly decay while propagating from the open boundary of Ω'_1 to Ω_1 [*Vladimirov*, 1971], numerical distortions of velocity snapshots within Ω should be small. Velocities reconstructed within the sub-domain $\Omega'_1 \backslash \Omega_1$, where the distortions are maximum possible, are excluded from further analysis.

[128] The extended domain Ω'_1 shown in Figure B1a was used to reconstruct $\hat{\mathbf{U}}$. The boundary of Ω' consists of six segments: two rigid boundary segments $\hat{\Gamma}_1$ and $\hat{\Gamma}_2$ along the 1000-m isobath, the rigid boundary segment $\hat{\Gamma}''_4$ along the equator, and three open-boundary segments $\hat{\Gamma}'_2$, $\hat{\Gamma}'_4$, and $\hat{\Gamma}'''_4$, as shown in Figure B1a. Boundary $\hat{\Gamma}''_4$ is considered to be a natural barrier for a geostrophic flow outside the western boundary currents. $\hat{\Gamma}'_4$ and $\hat{\Gamma}'''_4$ allow a nonzero transport across the southern boundary along the South American and African Coasts. *Busalacchi and Blanc* [1989] found similar boundary conditions to be acceptable for modeling large-scale off-equatorial currents.

[129] Following the work of *Chu et al.* [2003], we suppose zero-tangential velocity along any open-boundary segment of Ω'_1. A visual inspection of Argo float tracks (an example is shown in Figure B1b) also supports the boundary conditions for velocity at $\hat{\Gamma}'_4 \cup \hat{\Gamma}''_4 \cup \hat{\Gamma}'''_4$. The float trajectories indicate that there were no significant meridional fluxes across the equator outside of the western boundary current. *Richardson and Frantantoni* [1999] also pointed out that once in the equatorial band 3°S–3°N their Sound Fixing and Ranging (SOFAR) floats tended to stay there drifting long distances along the equator, except in the west where a direct connection to the meridional flow along the South American Coast was observed. However, Argo floats reveal significant meridional displacements in the ocean interior away from the equatorial band and intermediate boundary currents that was also noted by *Schmid et al.* [2003].

[130] Monthly temperature snapshots were reconstructed in the domain Ω'_1, which is to the north of 9°S (Figure B1c). Zero-diffusion heat flux across the rigid Γ_1, Γ_2, and the open Γ'_3 boundary segments is used as the boundary condition [*Ivanov et al.*, 2001].

[131] To understand the sensitivity of the obtained results to the choice of approximate open-boundary conditions, we additionally reconstructed the mid-depth circulation in a domain bounded by $\Gamma_1 \cup \Gamma_2 \cup \Gamma'_3$ (Figure B1c). For the

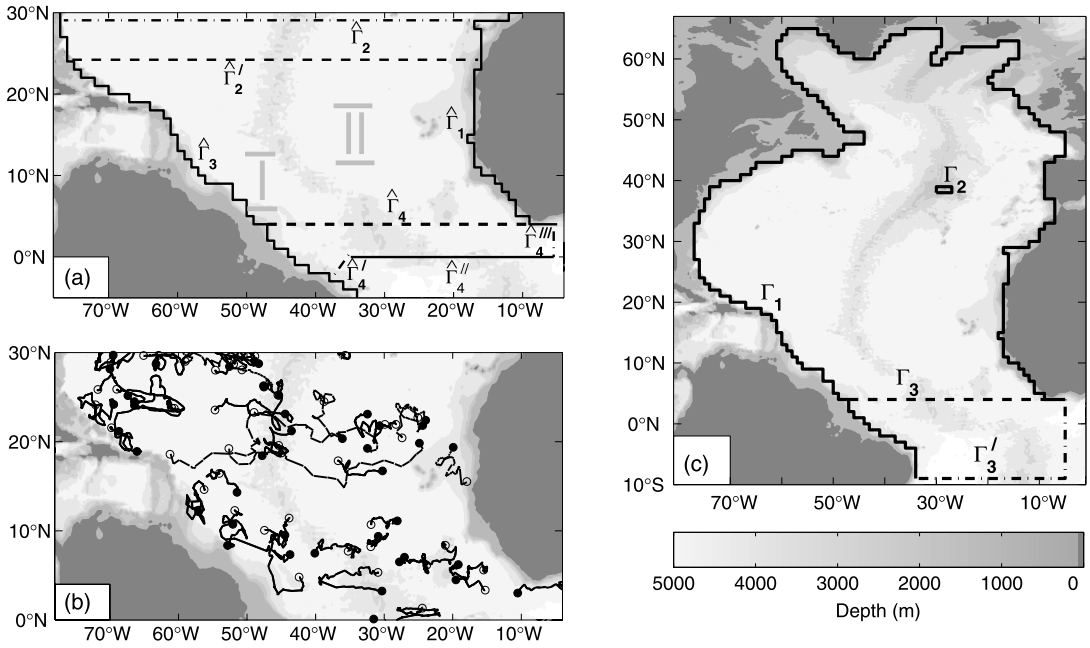

Figure B1. (a) Reconstruction domain for the tropical North Atlantic; (b) Argo floats tracks (drifted 300 days or longer) at 1000 and 1500 m between April 2004 and April 2005. Solid and white circles indicate points where floats were launched and their final positions, respectively; (c) reconstruction domain for the whole North Atlantic.

zonal band from 4° to 24°N, the difference between the velocity snapshots reconstructed in the whole North Atlantic and those computed only in this band is quite small. Even for the worst case shown in Figure B2, the root mean square difference between such snapshots is less than 14% and they have almost the same spatial structure. This (and other results not shown here) indicates a fast decay of the open-boundary-related error propagating from the shifted boundary into the reconstruction domain.

[132] The harmonic (Z_s) and basis (Ψ_k, Ξ_m) functions used in the reconstruction process satisfy

$$\Delta Z_s = 0, \quad \Delta\Psi_k = -\nu_k\Psi_k, \quad \Delta\Xi_m = -\mu_m\Xi_m, \qquad \text{(B1)}$$

where Δ is the horizontal Laplacian operator, and ν_k are its eigenvalues. Equation (B1) are solved with the following boundary conditions:

[133] (1) In the tropical region (4°–24°N)

[134] The computation domain Ω'_1 is shown in Figure B1a. Two harmonic functions Z_1 and Z_2 should be used in equation (1) because of three disconnected open-boundary segments: $\hat{\Gamma}'_2$, $\hat{\Gamma}'_4$, and $\hat{\Gamma}'''_4$. The boundary conditions are:

$$Z_1\Big|_{\hat{\Gamma}_1} = 1, \quad Z_1\Big|_{\hat{\Gamma}_3\cup\hat{\Gamma}''_4} = 0, \quad \mathbf{n}\cdot\nabla Z_1\Big|_{\hat{\Gamma}'_2\cup\hat{\Gamma}'_4\cup\hat{\Gamma}'''_4} = 0, \qquad \text{(B2)}$$

$$Z_2\Big|_{\hat{\Gamma}''_4} = 1, \quad Z_2\Big|_{\hat{\Gamma}_1\cup\hat{\Gamma}_3} = 0, \quad \mathbf{n}\cdot\nabla Z_2\Big|_{\hat{\Gamma}'_2\cup\hat{\Gamma}'_4\cup\hat{\Gamma}'''_4} = 0, \qquad \text{(B3)}$$

$$\Psi_k\Big|_{\hat{\Gamma}_1\cup\hat{\Gamma}_3\cup\hat{\Gamma}'_4} = 0, \quad \mathbf{n}\cdot\nabla\Psi_k\Big|_{\hat{\Gamma}'_2\cup\hat{\Gamma}'_4\cup\hat{\Gamma}''_4} = 0. \qquad \text{(B4)}$$

[135] (2) The whole North Atlantic

[136] The computation domain Ω'_2 bounded by $\Gamma_1 \cup \Gamma_2 \cup \Gamma'_3$ is shown in Figure B1c. This domain is multiconnected because of the presence of the Azores Plateau (Γ_2) and,

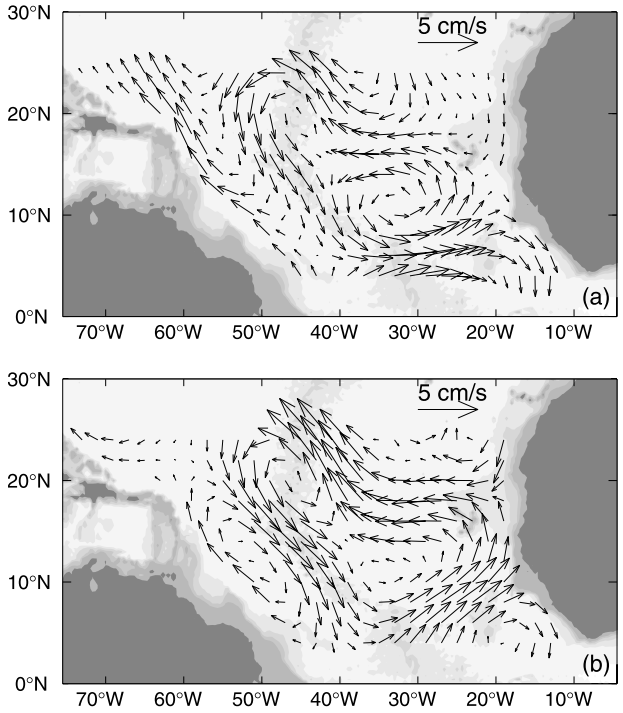

Figure B2. Mid-depth currents reconstructed from August–September 2004 data: (a) the whole North Atlantic and (b) only in the zonal band 4°N–24°N.

therefore, one harmonic function should be used in equation (1).

$$Z_1|_{\Gamma_1} = 0, \quad Z_1|_{\Gamma_2} = 1, \quad \mathbf{n} \cdot \nabla Z_1 \Big|_{\Gamma'_3} = 0, \tag{B5}$$

$$\Psi_k|_{\Gamma_1 \cup \Gamma_2} = 0, \quad \mathbf{n} \cdot \nabla \Psi_k \Big|_{\Gamma'_3} = 0, \tag{B6}$$

$$\mathbf{n} \cdot \nabla \Xi_m \Big|_{\Gamma_1 \cup \Gamma_2 \cup \Gamma'_3} = 0, \tag{B7}$$

where $\mathbf{n}$ is the unit positive vector normal to the boundary of domain Ω'_2.

[137] This is clear from equations (B1)–(B7) that the chosen basis functions allow us to satisfy the physical conditions at boundaries of appropriate extended domains.

[138] **Acknowledgments.** This research was supported by the Office of Naval Research and Naval Oceanographic Office for Peter Chu and Oleg Melnichenko. Leonid Ivanov thanks the National Science Foundation (NSF) for support through the award N-OCE-0530748. The Argo data were collected and made freely available by the International Argo Project and the national programs that contribute to it (http://www.Argo.ucsd.edu, http://Argo.jcommops.org). NCEP reanalysis data provided by the NOAA-CIRES ESRL/PSD Climate Diagnostic branch, Boulder, Colorado, USA, from their Web site at http://www.cdc.noaa.gov/ were used in the present study. Leonid Ivanov also thanks the Royal Society (Great Britain) for providing a grant for his visit to the Southampton Oceanographic Center (now National Oceanography Center). The authors thank the referees for their detailed reviews and constructive comments, which have lead to substantial improvements of the present paper.

References

Barnier, B. (1988), A numerical study on the influence of the Mid-Atlantic Ridge on nonlinear first-mode baroclinic Rossby waves generated by seasonal winds, *J. Phys. Oceanogr.*, *14*(3), 417–433.

Böning, C. W., and J. Kröger (2005), Seasonal variability of deep currents in the equatorial Atlantic: A model study, *Deep-Sea Res., Part 1*, *52*, 99–121.

Böning, C. W., and F. A. Schott (1993), Deep currents and the eastward salinity tongue in the equatorial Atlantic: Results from an eddy-resolving, primitive equation model, *J. Geophys. Res.*, *98*(C4), 6991–6999.

Brandt, P., and C. Eden (2005), Annual cycle and inter-annual variability of the mid-depth tropical Atlantic Ocean, *Deep-Sea Res., Part 1*, *52*, 199–219.

Busalacchi, A. J., and F. Blanc (1989), On the role of closed and open boundaries in a model of the tropical Atlantic Ocean, *J. Phys. Oceanogr.*, *19*, 831–840.

Chang, P. T., et al. (2005), Climate fluctuations of tropical coupled system. The role of ocean dynamics, *J. Climate*, *19*(20), 5122–5174.

Chelton, D. B., and M. G. Schlax (1996), Global observations of oceanic Rossby waves, *Science*, *272*, 234–238.

Chu, P. C., L. M. Ivanov, T. M. Margolina, T. P. Korzhova, and O. V. Melnichenko (2003), Analysis of sparse and noisy ocean current data using flow decomposition. I. Theory, *J. Atmos. Ocean. Technol.*, *16*, 478–491.

Chu, P. C., L. M. Ivanov, and T. M. Margolina (2004), Rotation method for reconstructing process and fields from imperfect data, *Int. J. Bifurc. Chaos*, *14*(8), 2991–2997.

Cipollini, P., D. Cromwell, M. S. Jones, G. D. Quartly, and P. G. Challenor (1997), Concurrent altimeter and infrared observations of Rossby wave propagation near 34°N in the Northeast Atlantic, *Geophys. Res. Lett.*, *24*(8), 889–892.

Cipollini, P., D. Cromwell, P. G. Chanselor, and S. Raffago (2001), Rossby waves detected in global ocean colour data, *Geophys. Res. Lett.*, *28*(2), 323–326.

Collins, C. A., L. M. Ivanov, O. V. Melnichenko, and N. Garfield (2004), California undercurrent variability and eddy transport estimated from RAFOS float observations, *J. Geophys. Res.*, *109*, C05028, doi:10.1029/2003JC002191.

Cox, M. D. (1987), An eddy-resolving numerical model of the ventilated thermocline: Time dependence, *J. Phys. Oceanogr.*, *13*, 1044–1056.

Eimoussaoui, A., M. Arhan, and A. M. Treguier (2005), Model-inferred upper circulation in the eastern tropics of the North Atlantic, *Deep-Sea Res., Part 1*, *52*, 1093–1116.

Engl, H. W., M. Hanke, and A. Neubauer (1996), *Regularization of Inverse Problems*, 321 pp., Springer, New York.

Eremeev, V. N., L. M. Ivanov, and A. D. Kirwan Jr. (1992), Reconstruction of oceanic flow characteristics from quasi-Lagrangian data. Part I. Approach and mathematical methods, *J. Geophys. Res.*, *97*, 9733–9742.

Fratantoni, D. M., and P. L. Richardson (1999), SOFAR float observations of an intermediate-depth eastern boundary current and mesoscale variability in the eastern tropical Atlantic Ocean, *J. Phys. Oceanogr.*, *29*, 1265–1278.

Freeland, H. J., P. B. Rhines, and T. Rossby (1975), Statistical observations of the trajectories of neutrally buoyant floats in the North Atlantic, *J. Mar. Res.*, *33*, 383–404.

Hill, K. L., I. S. Robinson, and P. Cipollini (2000), Propagation characteristics of extra-tropical planetary waves observed in the ATSR global sea surface temperature record, *J. Geophys. Res.*, *105*(C9), 21,927–21,945.

Herrmann, P., and W. Krauss (1989), Generation of propagation of annual Rossby waves in the North Atlantic, *J. Phys. Oceanogr.*, *19*(6), 727–744.

Gerdes, R., and C. Wübber (1991), Seasonal variability of the North Atlantic—a model inter-comparison, *J. Phys. Oceanogr.*, *21*, 1300–1322.

Gouriou, Y., B. Bourles, H. Mercier, and R. Chuchla (1999), Deep jets in the equatorial Atlantic Ocean, *J. Geophys. Res.*, *104*(C9), 21,217–21,226.

Ivanov, L. M., A. D. Kirwan Jr., and T. M. Margolina (2001), Filtering noise from oceanographic data with some applications for the Kara and Black Seas, *J. Mar. Syst.*, *28*(1–2), 113–139.

Jochum, M., and P. Malanotte-Rizzoli (2003), The flow of AAIW along equator, in *Inter-hemispheric Water Exchange in the Atlantic Ocean*, edited by G. I. Goni and P. Malanotte-Rizzoli, pp. 193–212, Elsevier Oceanographic Series, 68, Elsevier, New York.

Killworth, P. D., P. Cipollini, B. Mete Uz, and J. R. Blundell (2004), Physical and biological mechanisms for planetary waves observed in satellite-derived chlorophyll, *J. Geophys. Res.*, *109*, C07002, doi:10.1029/2003JC001768.

Krauss, W., and C. Wuebber (1982), Response of the North Atlantic to annual wind variations along the east coast, *Deep-Sea Res.*, *29*, 851–864.

Landa, P. S. (1996), *Nonlinear Oscillations and Waves in Dynamical Systems*, 564 pp, Springer, New York.

Levitus, S., T. P. Boyer, M. E. Coukright, T. O'Brien, J. Antonov, C. Dtephens, L. Stathoplos, D. Johnson, and R. Gelfed (1998), *Introduction. Vol. 1, World Ocean Database 1998: NOAA Atlas NESDIS 14*, 346 pp., U.S. Gov. Print. Off., Washington, D. C.

Li, X. (1996), Equatorially trapped waves and wave-induced mixing in the mid-depth Atlantic Ocean, Ph. D. dissertation, 166 pp., University of Texas A&M, Texas.

Molinari, R. L., S. L. Garzoli, and R. W. Schmitt (1999), Equatorial currents at 1000 m in the Atlantic Ocean, *Geophys. Res. Lett.*, *26*(3), 361–363.

Osychny, V., and P. Cornillon (2004), Properties of Rossby waves in the North Atlantic estimated from satellite data, *J. Phys. Oceanogr.*, *34*(1), 61–76.

Park, J. J., K. Kim, B. A. King, and S. C. Riser (2005), An advanced method to estimate deep currents from profiling floats, *J. Atmos. Ocean. Technol.*, *22*, 1294–1304.

Pedlosky, J. (1987), *Geophysical Fluid Dynamics*, 2nd ed., 625 pp., Springer, New York.

Perry, A. E., and M. S. Chong (1987), A description of eddying motions and flow patterns using critical point concepts, *Annu. Rev. Fluid Mech.*, 127–155.

Phylander, S. G., and R. C. Pacanowski (1980), The generation of equatorial currents, *J. Geophys. Res.*, *85*(C2), 1123–1136.

Polito, P. S., and P. Cornillon (1997), Long baroclinic Rossby waves detected by Topex/Poseidon, *J. Geophys. Res.*, *102*, 3215–3235.

Rabinovich, M. I., and D. I. Trubetskov (1989), *Oscillations and Waves: In Linear and Nonlinear Systems*, 1st ed., 604 pp., Springer, New York.

Reid, J. L. (1994), On the total geostrophic circulation of the North Atlantic Ocean: flow patterns, tracers, and transports, *Prog. Oceanogr.*, *33*, 1–92.

Richardson, P. L., and D. M. Frantantoni (1999), Float trajectories in the deep western boundary current and deep equatorial jets of the tropical Atlantic, *Deep-Sea Res., Part 2*, *56*, 305–333.

Rhines, P. (2004), Oceanic and atmospheric Rossby waves. A lecture for the Norman Phillips symposium at the annual Amer. Meteorological Society meeting. (Available at http://www.ocean.washington.edu/research/gfd/papers-rhines.html)

Schmid, C., Z. Garraffo, E. Johns, and S. L. Garzoli (2003), Pathways and variability at intermediate depths in the tropical Atlantic, in *Inter-hemispheric Water Exchange in the Atlantic Ocean*, edited by G. I. Goni

and P. Malanotte-Rizzoli, pp. 233–268, Elsevier Oceanographic Series, 68, Elsevier, New York.
Schmid, C., B. Bourles, and Y. Gouriou (2005), Impact of the equatorial deep jets on estimates of zonal transports in the Atlantic, *Deep-Sea Res., Part 2*, *52*, 409–428.
Schott, F. A., J. Fisher, and L. Stramma (1998), Transports and pathways of the upper-layer circulation in the western tropical Atlantic, *J. Phys. Oceanogr.*, *28*(10), 1904–1928.
Schouten, M. W., R. P. Matano, and T. P. Strub (2005), A description of the seasonal cycle of the equatorial Atlantic from altimeter data, *Deep-Sea Res., Part 1*, *52*, 477–493.
Semtner, A. J., and R. M. Chervin (1992), Ocean general circulation from a global eddy-resolving model, *J. Geophys. Res.*, *97*(C4), 5493–5550.
Stramma, L., and F. A. Schott (1999), The mean flow field of the tropical Atlantic Ocean, *Deep-Sea Res., Part 2*, *46*(1–2), 279–303.
Thierry, V., A.-M. Triguer, and H. Mercier (2004), Numerical study of the annual and semi-annual fluctuations in the deep equatorial Atlantic Ocean, *Ocean Model.*, *6*, 1–30.
Turchin, V. F., V. P. Kozlov, and M. S. Malkevich (1971), The use of mathematical-statistics methods for the solution of ill-posed problems, *Sov. Phys., Usp.*, *103*(3–4), 681–703.
Vapnik, V. N. (2006), *Estimation of Dependencies Based on Empirical Data*, 505 pp., Springer, New York.
Vladimirov, V. S. (1971), *Equations of Mathematical Physics*, 464 pp., CRC Press, Boca Raton, Fla.
Wang, L. P., and C. J. Koblinsky (1994), Influence of mid-ocean ridges on Rossby waves, *J. Geophys. Res.*, *99*(C12), 25,143–25,153.
Wang, L. P., C. J. Koblinsky, and S. Howden (2001), Annual Rossby wave in the Southern Indian Ocean: why does it ''appear'' to break down in the middle ocean?, *J. Phys. Oceanogr.*, *31*, 54–74.
Yang, J. (1999), A linkage for decadal climate variations in the Labrador Sea and the tropical Atlantic Ocean, *Geophys. Res. Lett.*, *30*, 1070–1073.
Yaglom, A. M. (1986), *Correlation Theory of Stationary and Related Random Functions*, vol. I, Basic Results, 526 pp., Springer, New York.

P. C. Chu, L. M. Ivanov, and O. V. Melnichenko, Department of Oceanography, Naval Postgraduate School, 833 Dyer Road, Room 328, Monterey, CA 93943, USA. (lmivanov@nps.navy.mil)
N. C. Wells, Southampton Oceanography Center, Southampton, United Kingdom, SO14 3ZH.